# CHAPTER 6 A DAMAGE CRITERION FOR DUCTILE CRACK INITIATION AND PLASTIC INSTABILITY

The AHS steels basically exhibited complex damage mechanisms, which make the prediction of material formability difficult. On the microscopic scale, microcracks can initiate during an early state of deformation and restrict the formability limit of material, in which failure is reached without any noticeable macroscopic localized necking. The aim of the works in this chapter is to develop the damage criteria, which can be used to predict ductile crack initiation and instability state of the AHS steel grade JAC780Y during forming operation. First, a hybrid experimental and numerical analysis was applied to determine the ductile crack initiation locus (DCIL). Tensile tests of various sheet sample geometries were experimentally carried out and crack onsets occurred during forming were identified by the direct current potential drop (DCPD) method. Subsequently, FE simulations of the corresponding tests were performed to evaluate local stress triaxialities and equivalent plastic strains of the critical areas. The damage curves (DCs) for both crack initiation and instability were generated. Additionally, the von Mises, Hill’48 and Yld2000–2d yield criterion were defined in the calculations in order to examine effects of the yield models on the resulted damage curves. The obtained DCs were also transformed to the strain based forming limit curves (FLCs). To verify applicability of the damage curves and FLCs for crack initiation and plastic instability, the Nakazima tests and forming test of an industrial part were performed.

## 6.1 Introduction

The automotive industries are being heavily forced to design and make vehicles under considerations of weight reduction, crash performance, energy saving and environmental aspect have been of special interest. Thickness reduction of steel sheets used in car bodies is desirable as it leads to vehicles that have low fuel consumption and $CO_2$ emission. On the other hand, passenger safety can be enhanced by applying steels with increased energy absorption ability. Thus, the steel grades with higher strength and ductility are simultaneously needed. To meet these requirements the advanced high strength (AHS) steel grades, such as dual phase (DP) steel, transformation induced plasticity (TRIP) steel and complex (CP) steel or ultra- high strength (UHS) steels like press hardened boron alloy steel have been continuously developed and employed [41,56]. The distinguished mechanical properties of the AHS steels are especially due to their microstructure characteristics and interactions between different phases. These complex microstructures result in sophisticated fracture behavior of the AHS steels. On the microscale, ductile damage of steels is governed by the void nucleation, growth and coalescence mechanism. In the dual phase steels, the ductile damage becomes more complicated. Voids could be induced by the debonding of phase boundaries between ferrite and martensite, brittle cracking of the hard phase and by inclusions or small precipitates, as shown by Uthaisangsuk et al. [56] and Lian et al. [64]. Otherwise, Lian et al. [64] and Lian et al. [104] reported that fractures of these steels were observed on the macroscale in the absence of strain localization or minimal post necking deformation. This would be a critical issue for part makers in the automotive industry. Since possibilities of the initiation of microcracks increased in such multiphase AHS steels, subsequent damage onset and evolution became more influential on the formability limits, in which fracture could even occur without any macroscopic localized necking [105]. Therefore, failure of the AHS steels in sheet metal forming processes is caused by competing or combined mechanisms of the local damage evolution and plastic instability. In this work, it has been aimed to develop a damage criterion for describing ductile crack initiation and plastic instability of the AHS steel sheets during deformation. Usually, some ductile damage models characterize the critical loading conditions by relating the equivalent strain to fracture using a function of those parameters, which represent the state of stress. Already in the 1960s, effects of the stress triaxiality on the equivalent plastic strain to ductile fracture were presented by McClintock [47] and Rice and Tracey [48]. It was shown that ductile fractures of metals were strongly dependent on the hydrostatic stress, by which growths of cylindrical and spherical voids were studied. Similar experimental investigations were done by Hancock and Mackenzie [51], Hancock and Brown [106] and Bao and Wierzbicki [50]. Dependencies of ductile crack initiation on the hydrostatic stress were introduced by Atkins [49]. Bao and Wierzbicki [50] verified that the mechanism of ductile crack initiation and fracture was different and depended on magnitude of the stress triaxiality. Hancock and Mackenzie [51] examined the effects of multi-axial stress-state on the effective plastic strain required to initiate ductile failure in three high strength steels. A series of tensile tests on pre-notched steel specimens was performed. It was stated that a function between the strains to failure or crack initiation and stress–state was a practical material properties. Tensile tests of various notched sheet samples were experimentally and numerically investigated in Bao and Wierzbicki (66) and Panich et al. (67). It was found that crack occurred in the middle of smooth notch cylindrical specimen, where the highest stress triaxiality and lowest plastic strain were determined. In contrast, crack initiated close to the surfaces of sharp notch specimens. To obtain a damage criterion considering the entire range of state of stress a comprehensive experiment is necessary. In addition, accompanying FE simulations have to be carried out to evaluate the effective plastic strain and triaxiality values for the region of crack initiation. In [66] a series of experiments including upsetting test, shear test and tensile tests with various notched samples was carried out for an aluminum alloy, in which the dependence of material ductility on the stress triaxiality was discussed. In this work, a wide range of the stress triaxiality from –0.33 to 0.95 could be examined. Furthermore, Dunand and Mohr [62] performed tensile tests of sheet samples with a central hole and different circular notches. The equi–biaxial punch test was conducted for achieving fracture induced by the stress triaxialities of about 0.3 and 0.66.

In general, the forming limit diagram (FLD) introduced by Keeler [107] and Goodwin [28] was often used in sheet forming industries for optimizing forming process and exploring material formability on the basis of necking phenomenon. The localized necking or plastic instability has been described by various theoretical models, as demonstrated in [41]. The FLD predictions by such models were acceptable for the conventional steel alloys. However, applications of the FLD for evaluating forming behavior of the multiphase high strength steels have become problematic due to the early crack initiation. In these steels with multiphase microstructures, local strain distribution with strong gradients developed during the forming operations, which resulted in significant damages on the microscale. This consequently affected the macroscopic behavior of components when cracks were formed [105]. Principally, material failure of sheet metals is controlled by two decisive factors, namely, the damage accumulation and plastic instability. Highly ductile steels typically exhibited failure as a result of the plastic instability. In case of the AHS steels, the microscopic damage played an important role during plastic deformation and their failures took place because of damage evolution or damage and plastic instability in concurrence. Obviously, in the AHS steels crack initiation could arise prior to necking, as reported by

Tasan et al. [108]. Recently, various ductile fracture criteria have been developed for evaluating material formability. For example, Bao and Wierzbicki [50] and Bai and Wierzbicki [75] introduced the failure criteria obtained by intensive experiments using different sample geometries. These formability criteria were based on the macroscopic fracture, which was likely too late in sheet metal forming of the AHS steels. Otherwise, the FLDs were directly derived from the developed fracture criteria, as shown in Li et al. [109]. Hereby, accuracy of the FLDs could be improved, since deformation zone due to the shear stress was taken into account, but they were still related to the macroscopic fracture. A tool for describing both ductile crack initiation and plastic instability during cold forming of the multiphase sheet steels is thus necessary.

The effects of anisotropic yield behavior of some AHS steels on predicted plastic deformation and forming limits were investigated by Lee et al. [84], Kim et al. [111], Kuwabara et al. [85] and Panich et al. [67]. Lee et al. [84] conducted the uniaxial tension, in–plane biaxial test for determining anisotropic properties of the DP590 steel sheets. It was found that the Yld2000-2d yield criterion incorporating parameters from the biaxial stress state predicted the thickness strains more accurate than other criteria. The limiting dome height (LDH) formability tests and respective FE simulations were performed by Kim et al. [111]. Resulted experimental and predicted punch load–displacement curves were compared and sheet thickness variations after forming were evaluated. Obviously, the Yld2000-2d model with anisotropy values regarding the biaxial state provided noticeably improved predictions.Kuwabara et al. [85] investigated deformation behavior of the DP780 steel grade 780 under hole expansion forming. It was demonstrated that the Yld2000–2d yield function with the *M*–exponent value of 4 more precisely predicted experimental results than the conventional von Mises and Hill’48 model.

In this work, damage curves for representing crack initiation and plastic instability of the high strength steel grade JAC780Y were determined as failure thresholds. Tensile tests of the samples with various shapes and corresponding FE simulations were carried out. During the tests, the direct current potential drop (DCPD) method and the maximum loading state were considered, in which the instants of crack initiation and localized necking or instability were identified, respectively. By this manner, the local stress triaxialities and equivalent plastic strains of the critical areas were determined. The von Mises, Hill’48 and Yld2000–2d yield criteria were applied in FE calculations in order to investigate the effects of yield surface on the resulted damage curves. The uniaxial tension, disk compression and hydraulic bulge test were performed for obtaining normalized flow stresses and *r*-values for the yield functions. To verify the obtained failure curves and FLCs based on the crack initiation and plastic instability, forming tests of the Nakazima samples and the industrial part were carried out. The predictions of material failure of the examined steel were compared with the experimental results and discussed.

## 6.2 Finite Element Simulations

To evaluate stress triaxialities and plastic strains for constructing damage curves, FE simulations of the tensile tests of different sample types were performed. The various geometries of the tensile samples caused different stress triaxialities in the material during deformation. 4–node shell elements with reduced integration point (S4R) and uniaxial tensile load as boundary condition were applied. Elastic–plastic material behavior, rate–independent hardening according to the Swift law and different yield functions of von Mises, Hill’s 48 and Yld2000–2d model were defined. Force – displacement curves from the experiments and FE simulations of the U– notch sample, as shown in Figure 6.1(b), were compared. Hereby, the FE results were verified and the point of time or loading condition when crack initiation took place in the experiments was identified. It was found that the experimentally measured and calculated curves were in acceptable agreement for all sample shapes. The effects of the yield functions could be generally observed from slight deviations between the calculated force–displacement curves, as seen in Figure 6.1(b). By comparing the FE results to the experiments, stress triaxialities and equivalent plastic strains were determined from critical areas of the samples at the instance of crack initiation. The distribution of the stress triaxiality and equivalent plastic strain in the middle of each sample along the x–path in Figure 6.2 and Figure 6.3 were examined. The notch shapes caused different irregular local stress and strain developments on the samples. Figure 6.2 and Figure 6.3 illustrate the distributions of calculated equivalent plastic strains on the deformed samples. The maximum plastic strains for the C– and radius–notch sample were observed at the sample edges. Fractures of the pure shear and combined loading sample took place at earlier states than the other samples with larger local plastic strains in the critical area. From the results in Figure 6.3, all other notched tensile samples also exhibited the maximum plastic strains at the edges, where crack initiation occurred. The U–notch sample showed premature failure due to the extreme notch shape. The central hole and elliptical hole sample had crack initiation at the hole edges according to the observed maximum plastic strain. With respect to the used notch shapes, different stress triaxiality values were obtained. The samples with sharper notch shapes provided higher stress triaxialities. The maximum stresses occurred in the middle area, while the maximum plastic strains resulted at the sample edges. The maximum plastic strains for the average stress triaxiality values corresponding to each state of stress or sample geometry were then gathered, from which damage curves based on various yield criteria for crack initiation were generated.

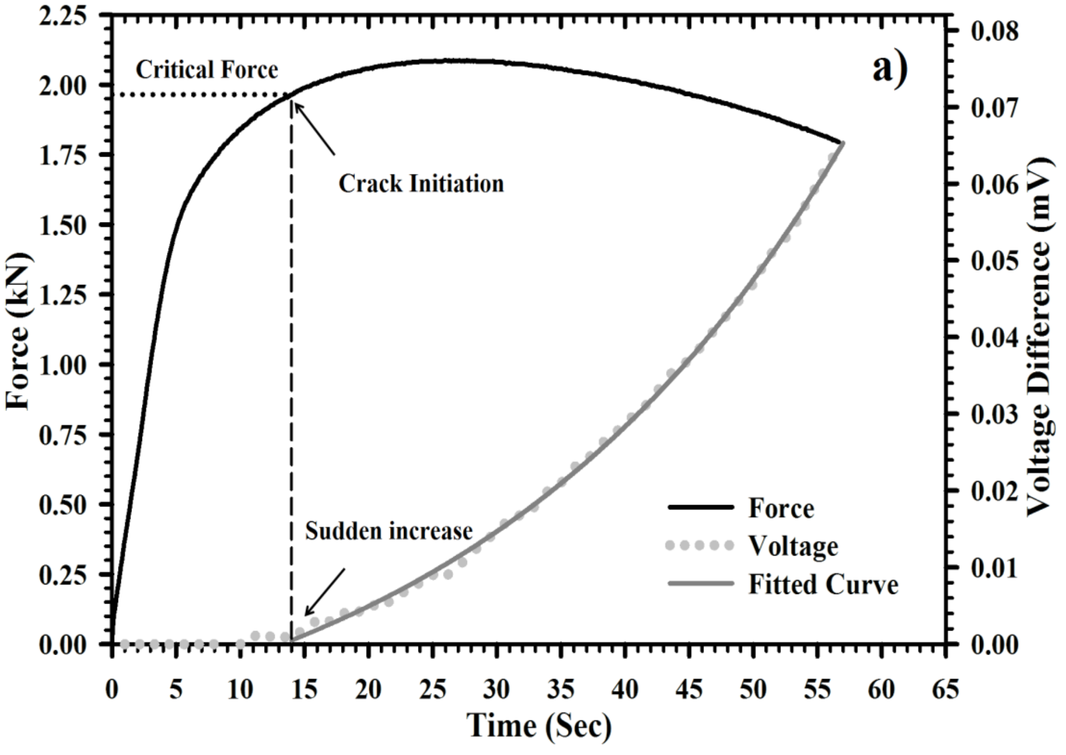

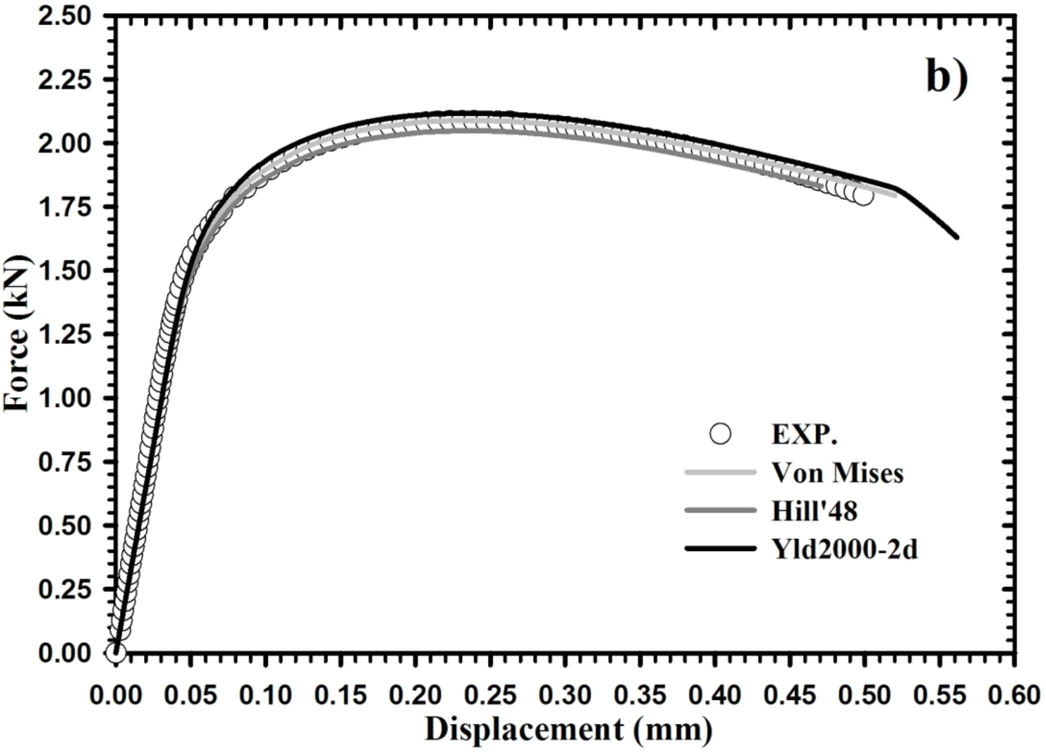

**Figure 6.1** (a) Experimentally determined force and electric potential difference versus time and (b) experimentally determined and predicted force - displacement curves of the U - notch sample

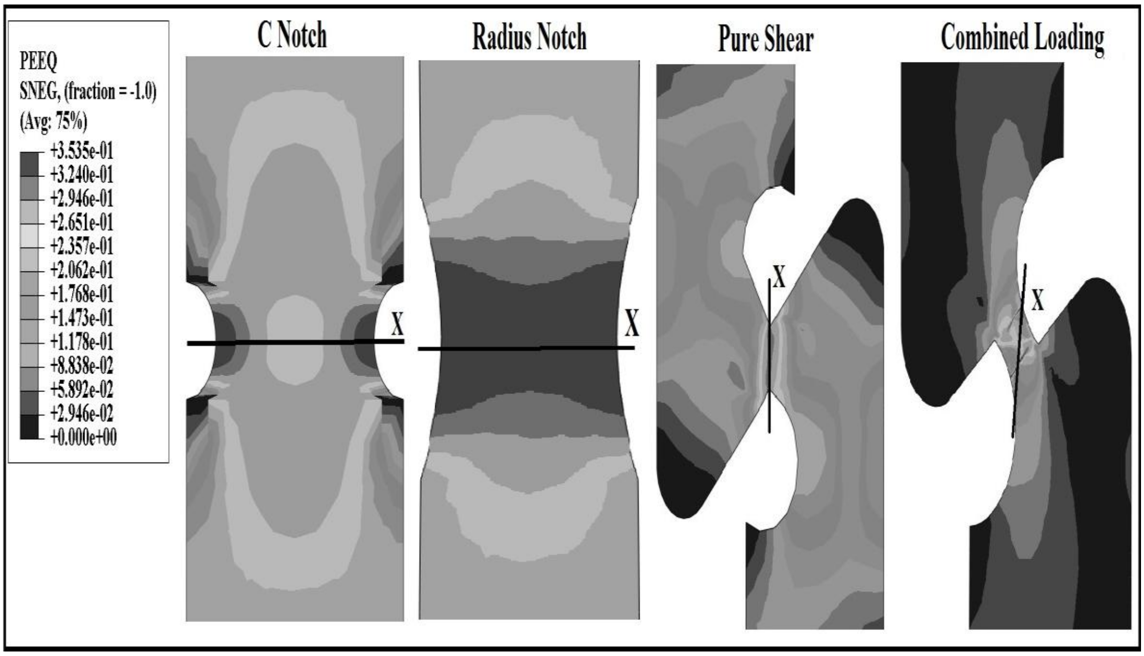

**Figure 6.2** Calculated strain distributions on the C–, radius–notch, pure shear and combined loading samples

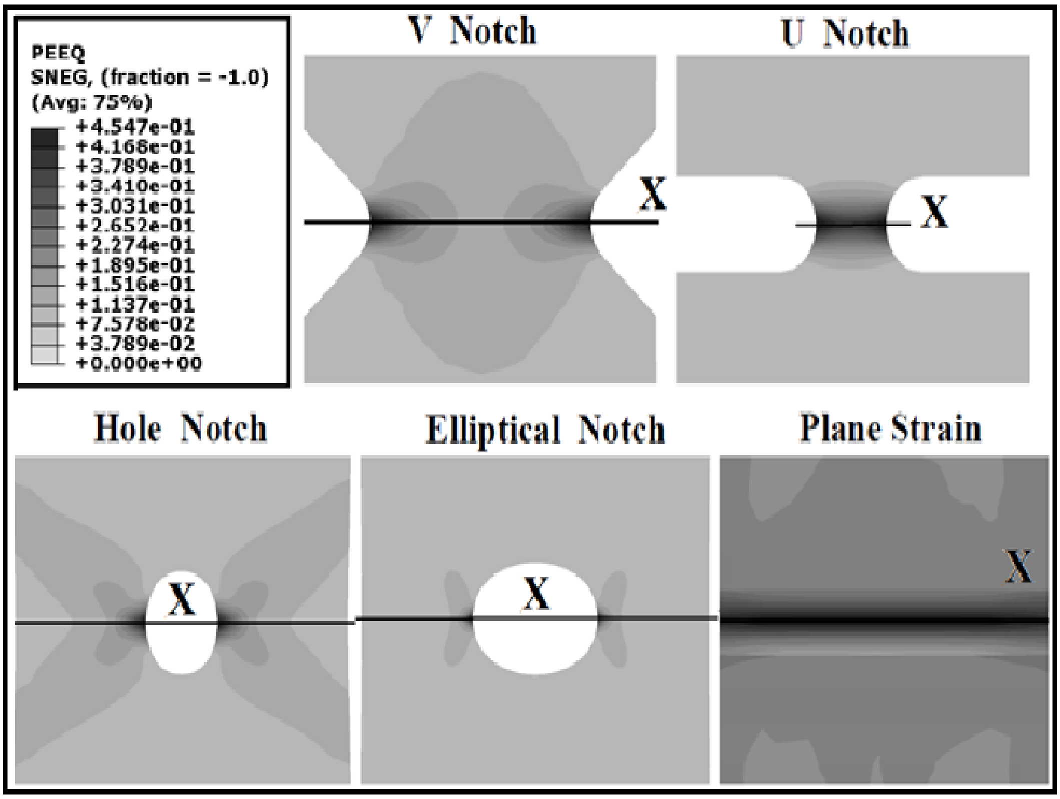

**Figure 6.3** Calculated strain distributions on the V–, U–notch, central hole, elliptical hole and plane strain samples

By this means, stress triaxialities and critical plastic strains were determined for all used tensile samples. The force–displacement curves and the potential difference curves obtained for the tensile samples with V–, radius–notch and combined loading (CL) sample were illustrated in Figure 6.4(a) – Figure 6.6(a). Figure 6.4(b) – Figure 6.6(b) demonstrate the experimentally determined and predicted force–displacement curves of the samples by applying different yield criteria in comparison. It could be seen that the force–displacement curves calculated by using the yield criteria in combination with the Swift hardening law were fairly in agreement with the experimental curves up to states of necking. The predicted curves a little bit overestimated the experimental ones before the maximum loads due to local damages taking place in the experiments. The damage onset and damage evolution during plastic deformation led to a prior softening of the examined steel, as reported by Lian et al. [64]. There were slight deviations between the predicted force–displacement curves using different yield criteria. It could be observed that the curves from FE simulations coupled with the Yld2000–2d model achieved higher displacements than the other models, in which large deformation was more properly described. An abrupt increase of the voltage difference curves indicated the state, when void coalescence and consequent crack initiation occurred. Note that various sample notch shapes established different increasing voltage characteristics during plastic deformation. In some cases, change in slope of the voltage difference curves needed to be analyzed. As aforementioned, stress triaxiality and plastic strain values along the x–path in the middle of each sample, where damage onset was anticipated, were examined. Then, the maximum plastic strains with corresponding average stress triaxialities were evaluated.

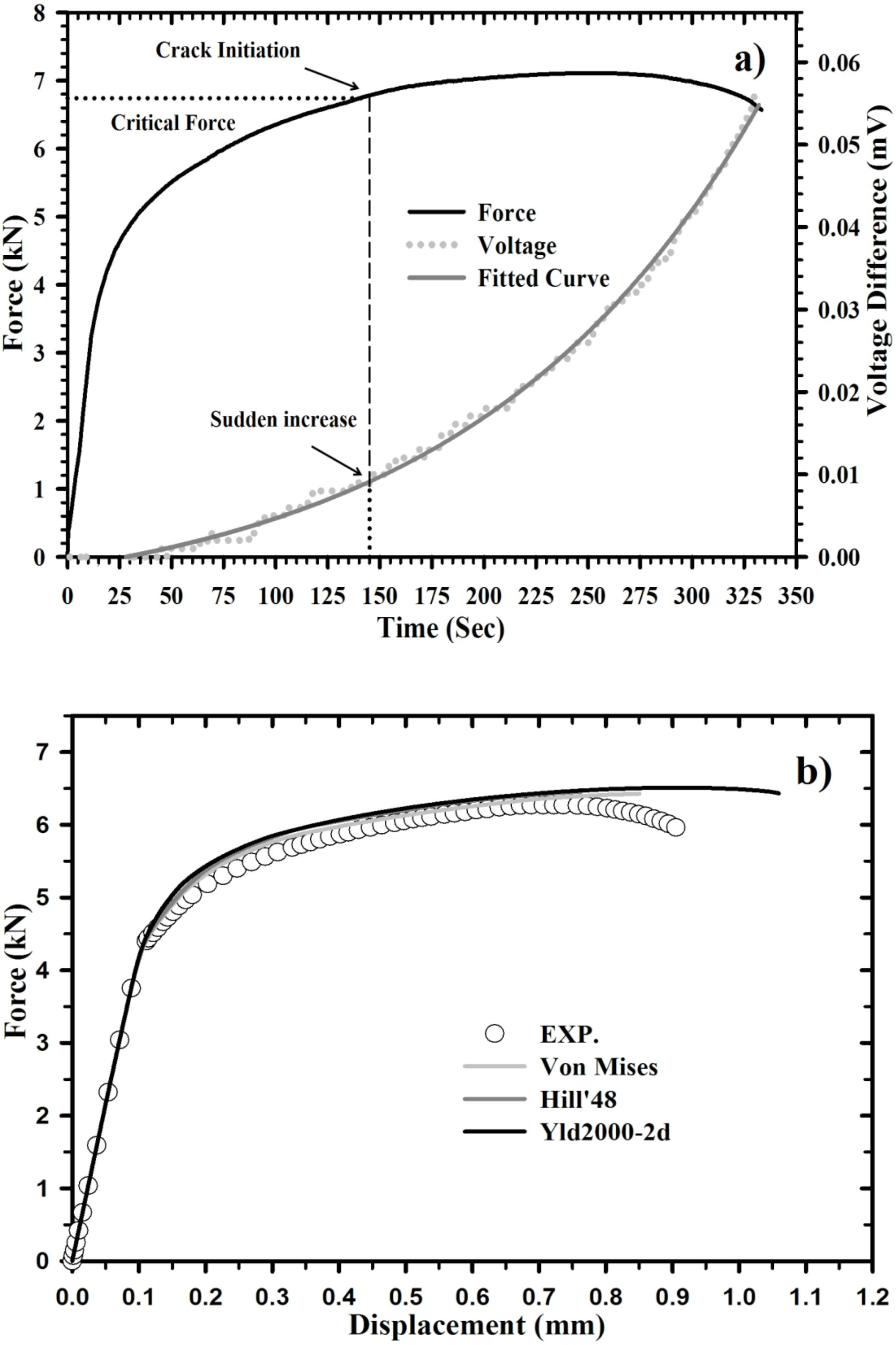

**Figure 6.4** (a) Experimentally determined force and electric potential difference versus time and (b) experimentally determined and predicted force-displacement curves of the V-notch sample.

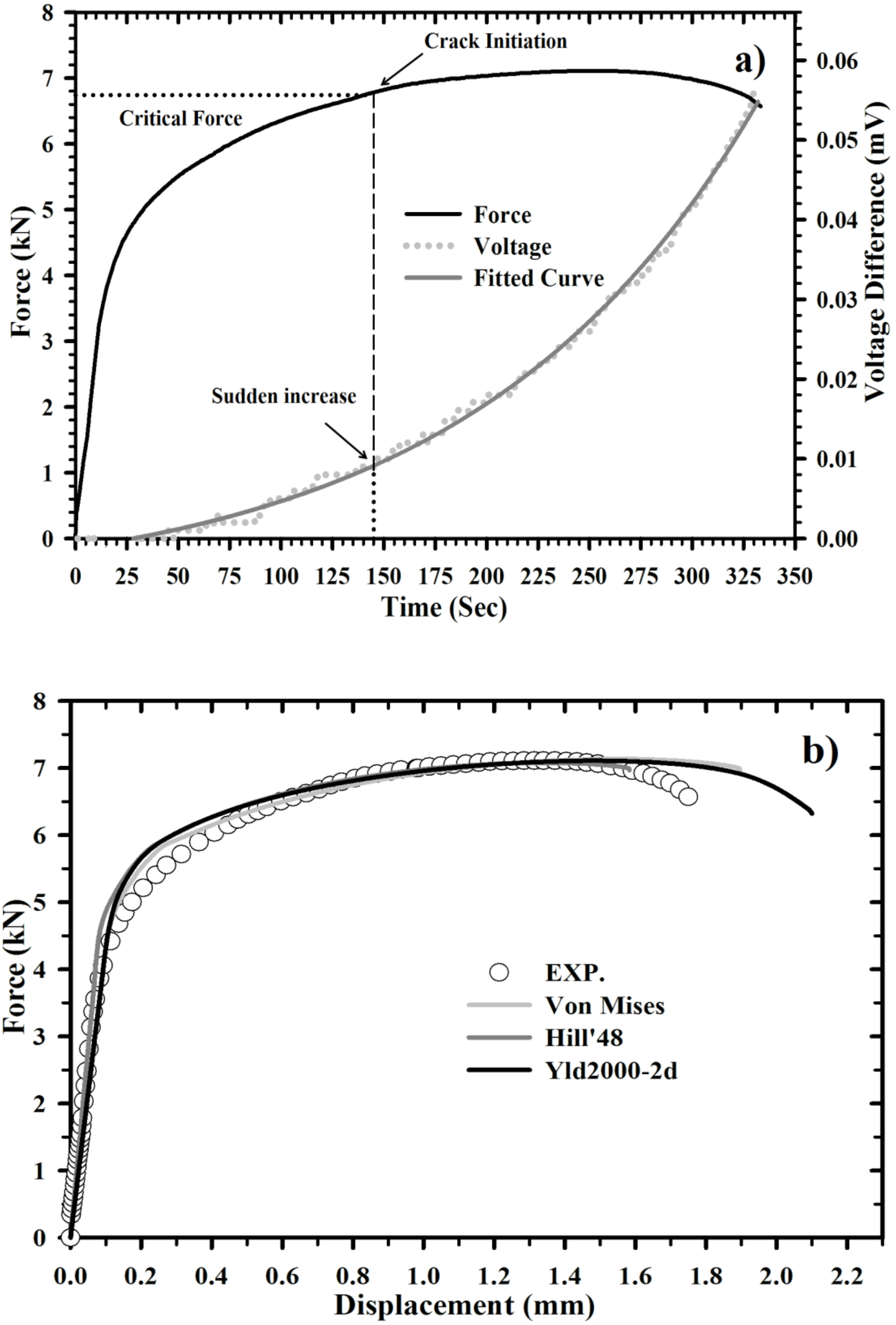

**Figure 6.5** (a) Experimentally determined force and electric potential difference versus time and (b) experimentally determined and predicted force-displacement curves of the radius-notch sample

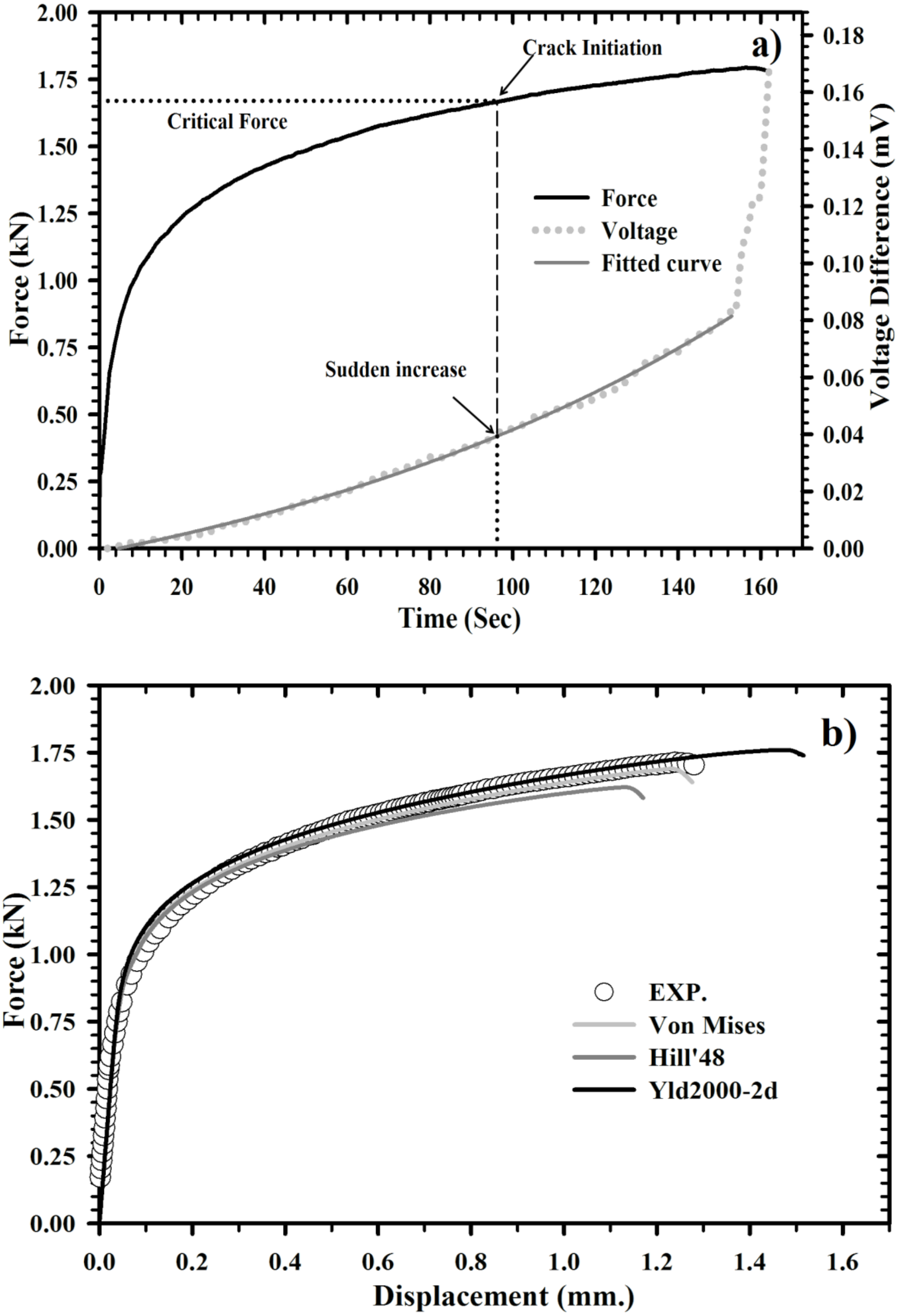

**Figure 6.6** (a) Experimentally determined force and electric potential difference versus time and (b) experimentally determined and predicted force-displacement curves of the CL sample

Figure 6.7(a) to Figure 6.7(c) depicts the experimentally determined force and electric potential difference versus time from the elliptical hole (EL), central hole (H) and plane strain (PL) samples. Similar trends of the curves for the El and H samples were found, since the states of stress induced by both samples were within the same range. Obviously, the potential difference curves of the CL, EL and H samples abruptly increased when localization occurred, because void volume fractions in such samples were likely high. The plane strain sample showed entirely different voltage characteristics as thickness in the middle of these samples was smaller than other samples.

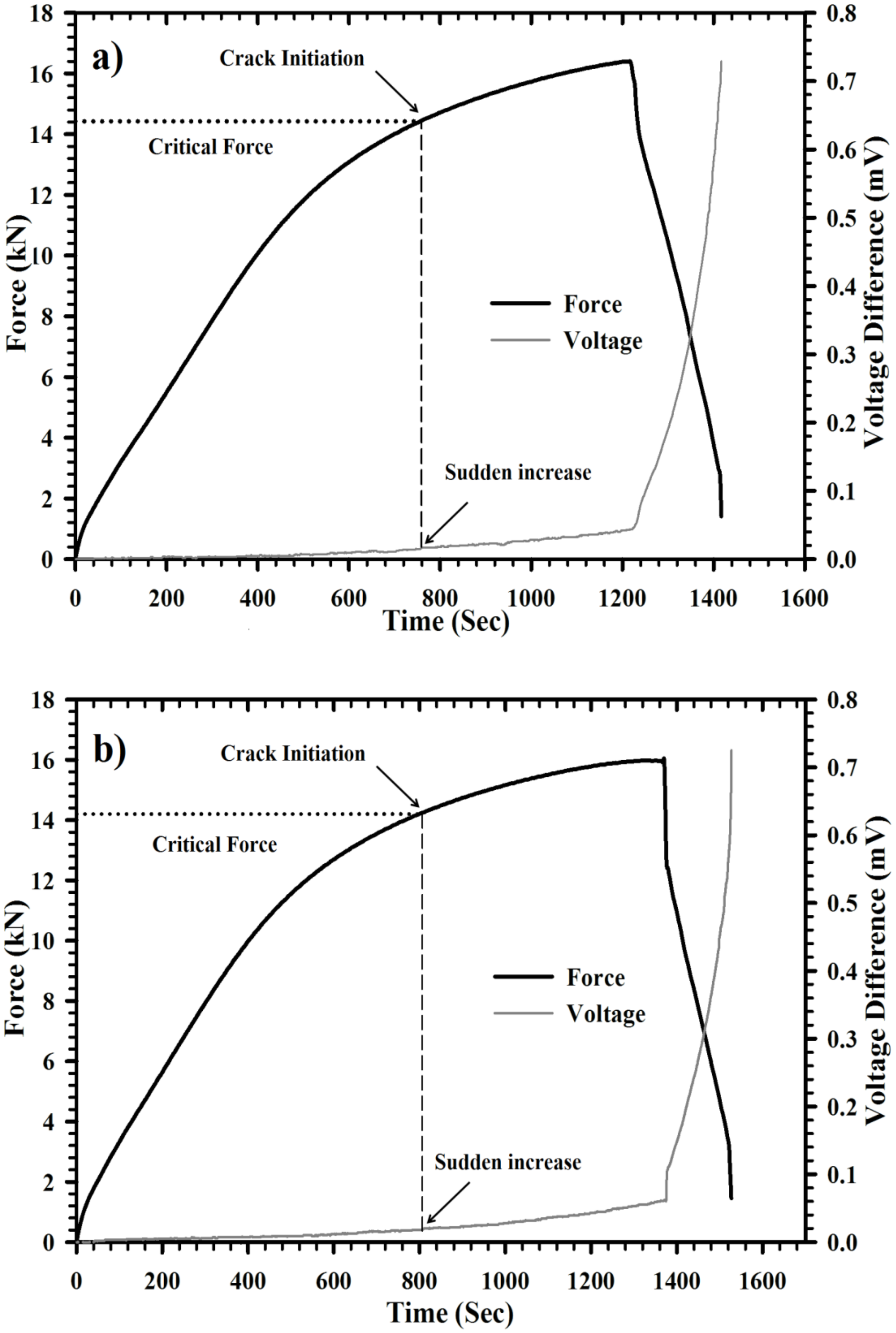

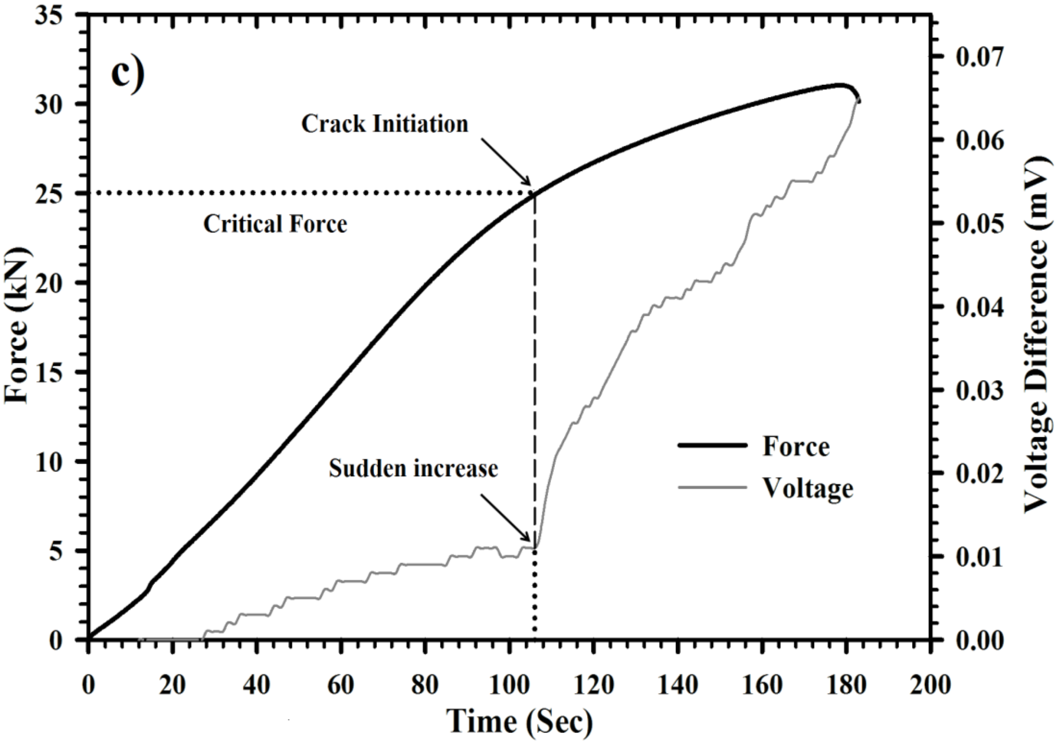

**Figure 6.7** Experimentally determined force and electric potential difference versus time of the (a) EL, (b) H and (c) Plane Strain samples

## 6.3 Results and discussion

The stress triaxialities and critical plastic strains determined from the FE simulations of all notched test samples at the crack initiation states were taken to construct a damage curve for the DP steel grade JAC780Y, as seen in Figure 6.8(a). Three different damage curves were shown as obtained from the FE results applying different yield functions. Apparently, the pure shear (PS) and combined shear and tension loading (CL) samples provided the low stress triaxiality values of 0.02 and 0.15, respectively. In contrast, the other samples exhibited higher stress triaxiality range between 0.3 and 0.62. The highest stress triaxiality was given by the plain strain (PL) sample. There were distinct deviations between the determined damage curves, especially in the middle and low stress triaxiality ranges. The damage curve according to the Yld2000–2d yield function showed slightly higher plastic strains than those based on the Hill’48 and von Mises yield model. In the low stress triaxiality range, the identified critical plastic strains from the Yld2000–2d model were much higher than that of other models. The obtained damage curves for crack initiation exhibited similar trends in all stress triaxialities ranges as those reported by Bao and Wierzbicki [50] for aluminum alloys. Furthermore, damage curves of AHS steel sheets were established by Li et al. [109] and Li and Wierzbicki [110], in which calculations were indeed performed on the basis of final fracture states.

### 6.3.1 Application to Nakazima test

The conventional Nakazima stretch–forming test of the four different shape samples, called B15, B30, B75 and B115, as shown in Figure 6.9, were experimentally carried out and simulated in order to validate the determined damage curves. Each sample shape represented individual in plane states of stress in the range between 0.33 and 0.66. For FE simulations of the Nakazima test, S4R shells, Swift hardening law, and three different yield functions, namely, von Mises, Hill’48 and Yld2000–2d were applied. Firstly, punch force–displacement curves predicted by the simulations were compared with those from the experiments for verifying the FE results of all used samples, as illustrated in Figure 6.10. The force–displacement curves calculated by using different yield functions exhibited some deviations from the experimental results. For the small samples, B15 and B30, the predicted force–displacement curves by all yield criteria were more accurate. However, in case of the large B75 and B115 samples, the calculated curves by the Yld2000–2d model a bit overestimated, while the curves by other yield models underestimated as the punch strokes increased. This could be due to the effects of friction between sample and punch. The stress–strain paths of the critical element, at which crack initiation was supposed, were calculated by the FE simulations and they were then plotted together on the determined damage curves, as demonstrated in Figure 6.8(b) – Figure 6.8(e) for the results obtained from the B15, B30, B75 and B115 samples, respectively. The stress–strain paths predicted by the Hill’48 and von Mises model were similar and slightly differed from those paths by the Yld2000–2d model. At the beginning of deformation, stress triaxiality continuously increased with plastic strain until reaching a certain value. Afterwards the stress triaxiality remained almost constant with increasing strains and represented each dominated stress state. The stress–strain paths of the B15 sample resulted in the stress triaxiality range of 1/3 or uniaxial state of stress. On the other hand, the B115 sample showed the stress–strain paths exactly in the biaxial state of stress ($\eta = 2/3$). Obviously, deviations between the stress–strain paths by different yield functions were larger from the deformation start and then became minimal when the stress triaxialities just approached the constant values. Note that these results were in contrary to the case of the B75 sample, in which the plane strain state governed. The discrepancies were much larger when the stress triaxiality achieved the steady state. The calculated stress–strain paths significantly depended on the state of stress and the yield function that could subsequently affect the failure prediction.

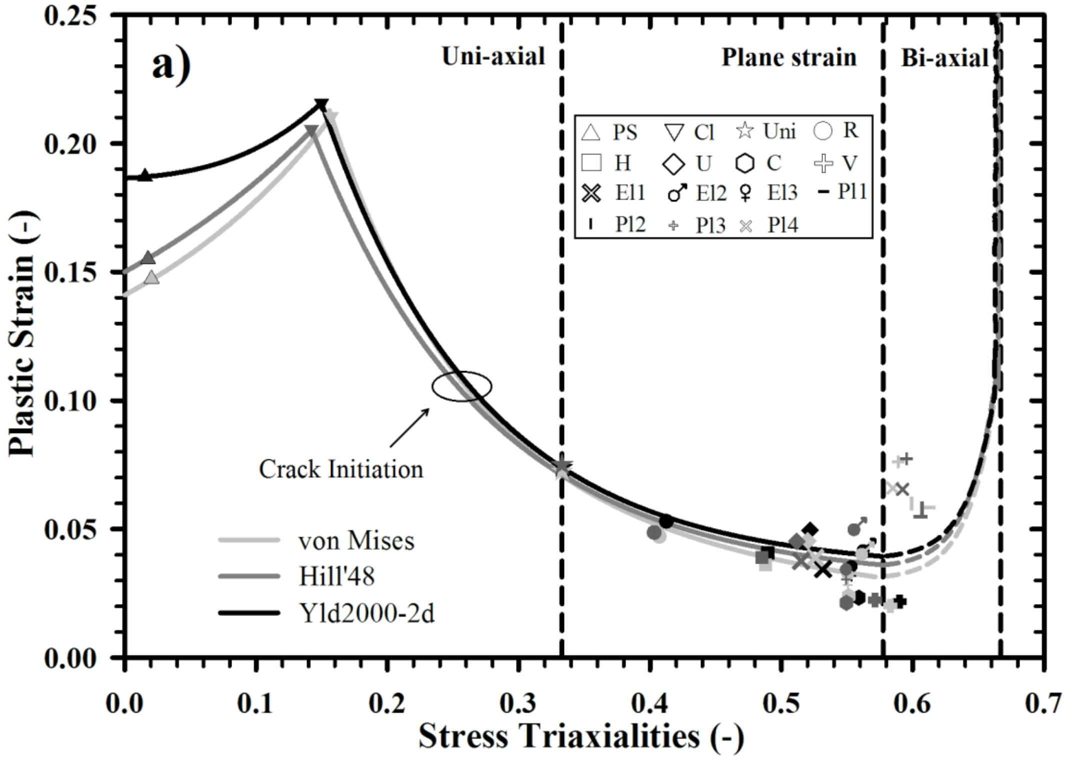

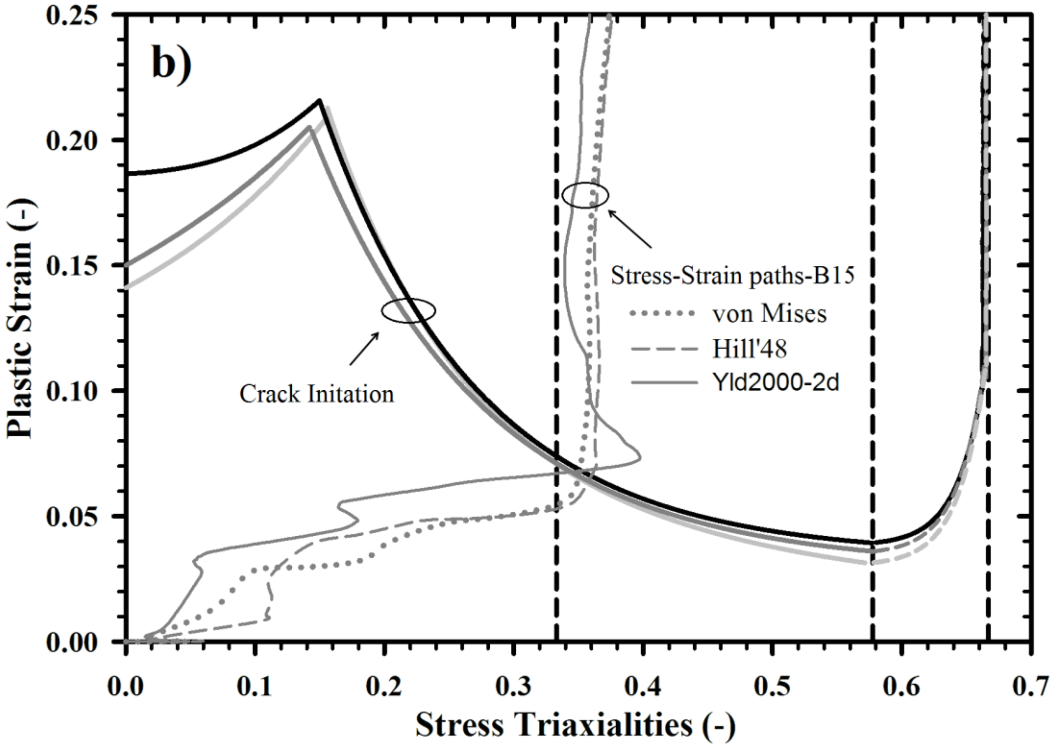
b)
Stress-Strain paths-B15
von Mises
Hill'48
Yld2000-2d
Crack Initation
Plastic Strain (-)
Stress Triaxialities (-)
0.00
0.05
0.10
0.15
0.20
0.25
0.0
0.1
0.2
0.3
0.4
0.5
0.6
0.7

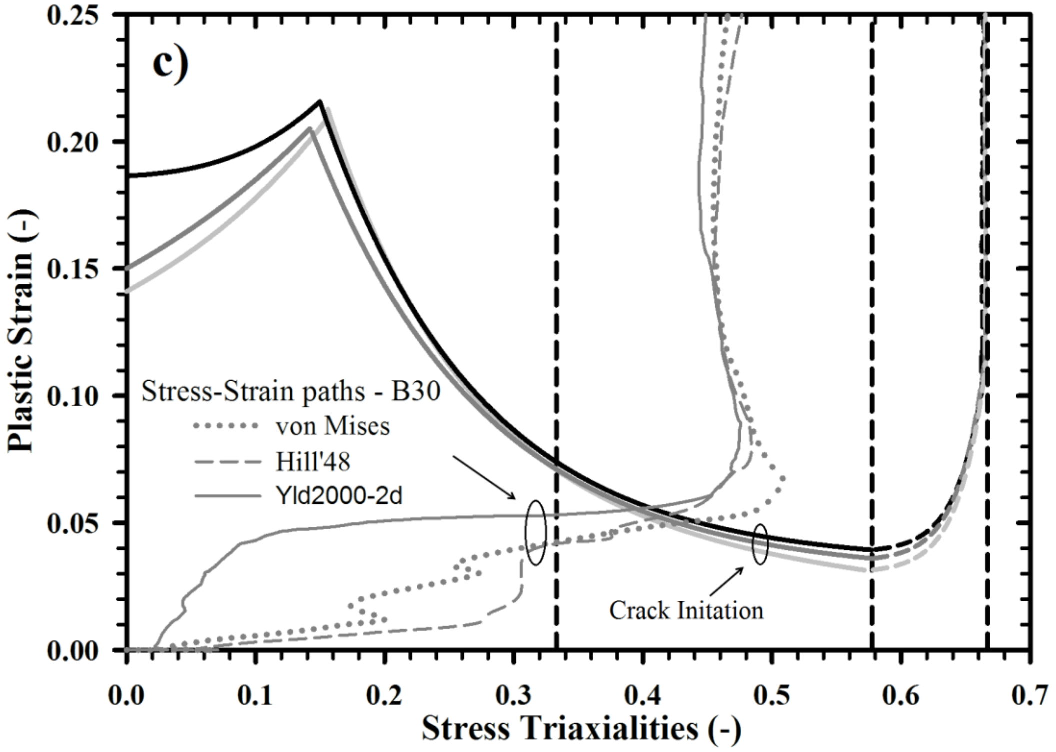
c)
Stress-Strain paths - B30
von Mises
Hill'48
Yld2000-2d
Crack Initation
Plastic Strain (-)
Stress Triaxialities (-)
0.00
0.05
0.10
0.15
0.20
0.25
0.0
0.1
0.2
0.3
0.4
0.5
0.6
0.7

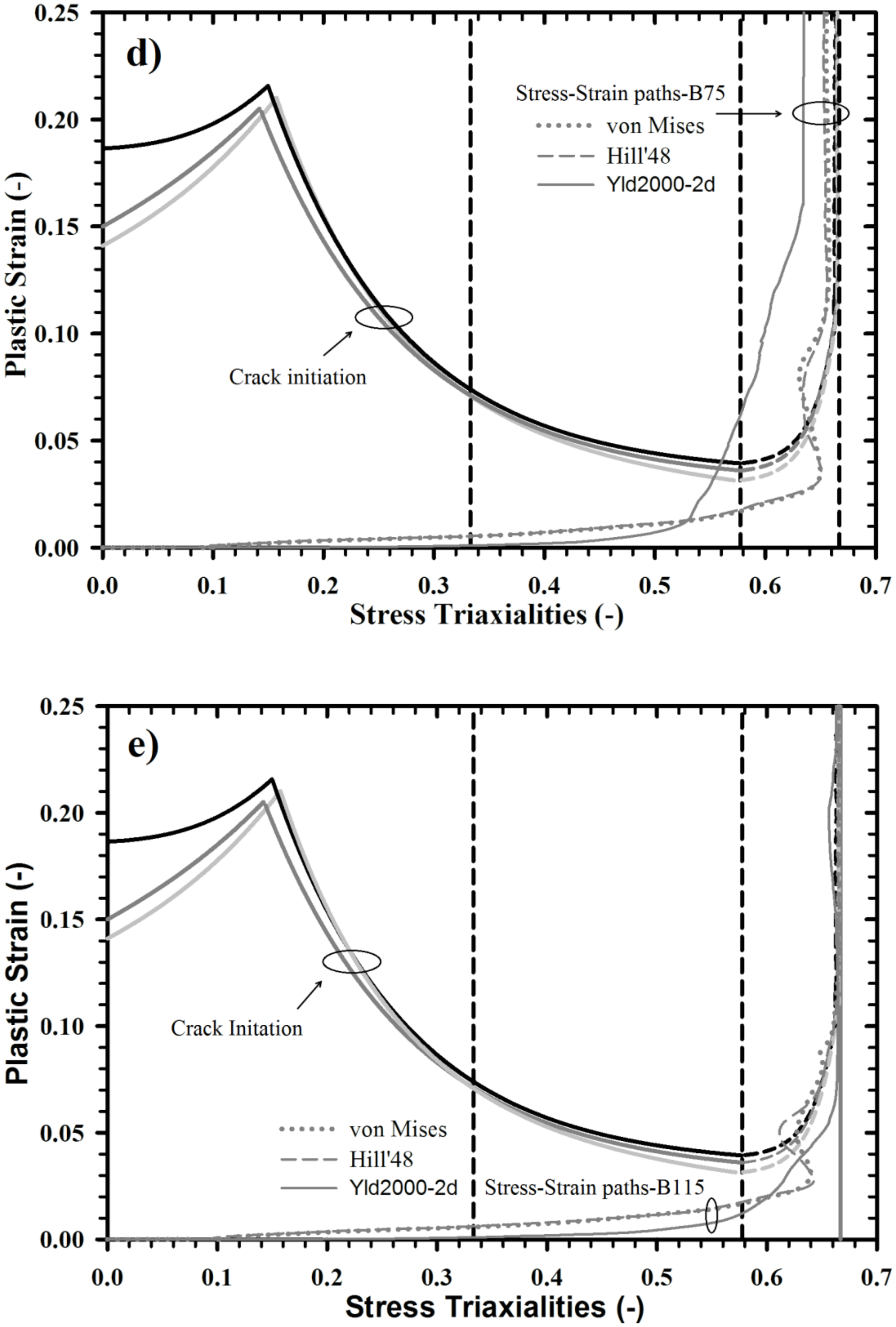

**Figure 6.8** (a) Determined damage curves for crack initiation using different yield criteria and stress–strain paths from the Nakazima samples (b) B15, (c) B30, (d) B75 and (e) B115 calculated using different yield criteria in comparison with the damage curves for the investigated DP steel

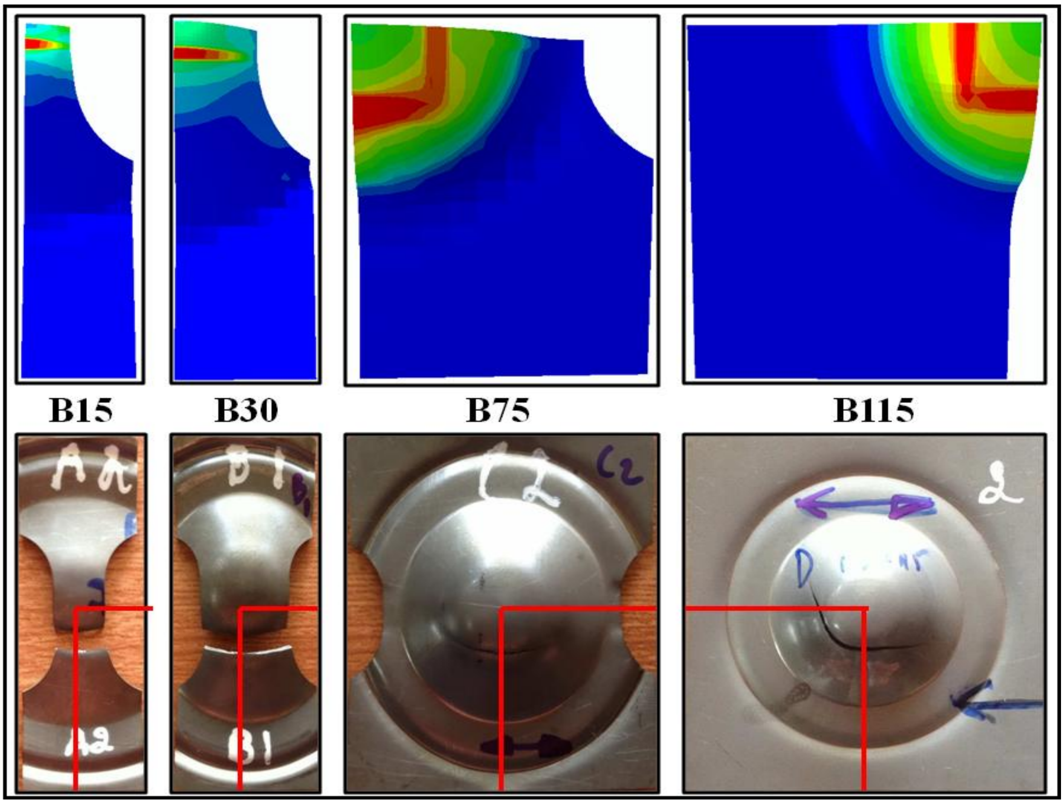

**Figure 6.9** Deformed Nakazima samples at failure state from the experiments and FE simulations

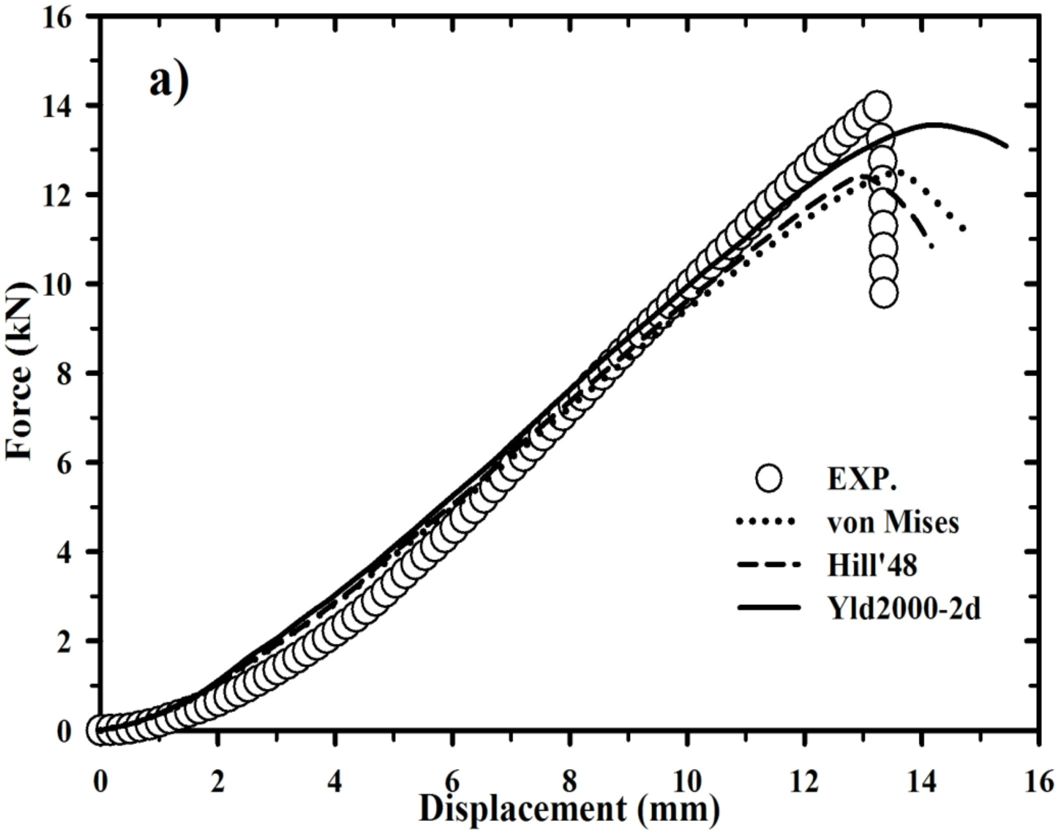

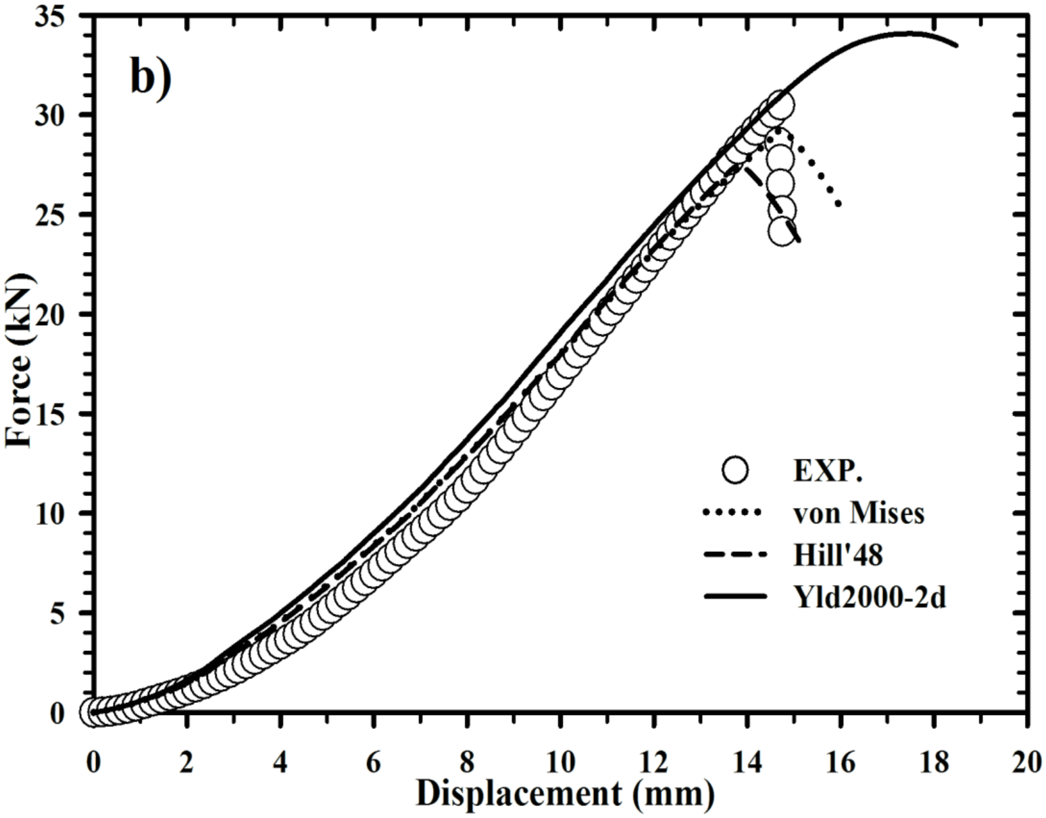
b)
Force (kN)
0
5
10
15
20
25
30
35
Displacement (mm)
0
2
4
6
8
10
12
14
16
18
20
EXP.
von Mises
Hill'48
Yld2000-2d

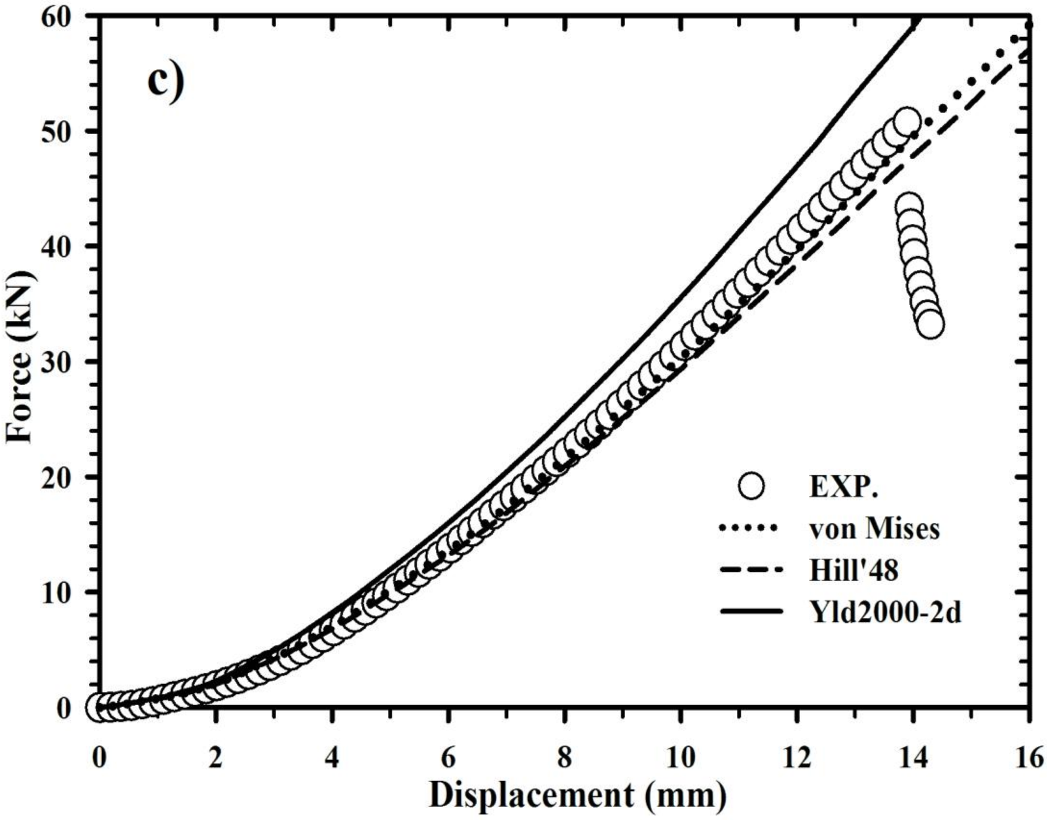
c)
Force (kN)
0
10
20
30
40
50
60
Displacement (mm)
0
2
4
6
8
10
12
14
16
EXP.
von Mises
Hill'48
Yld2000-2d

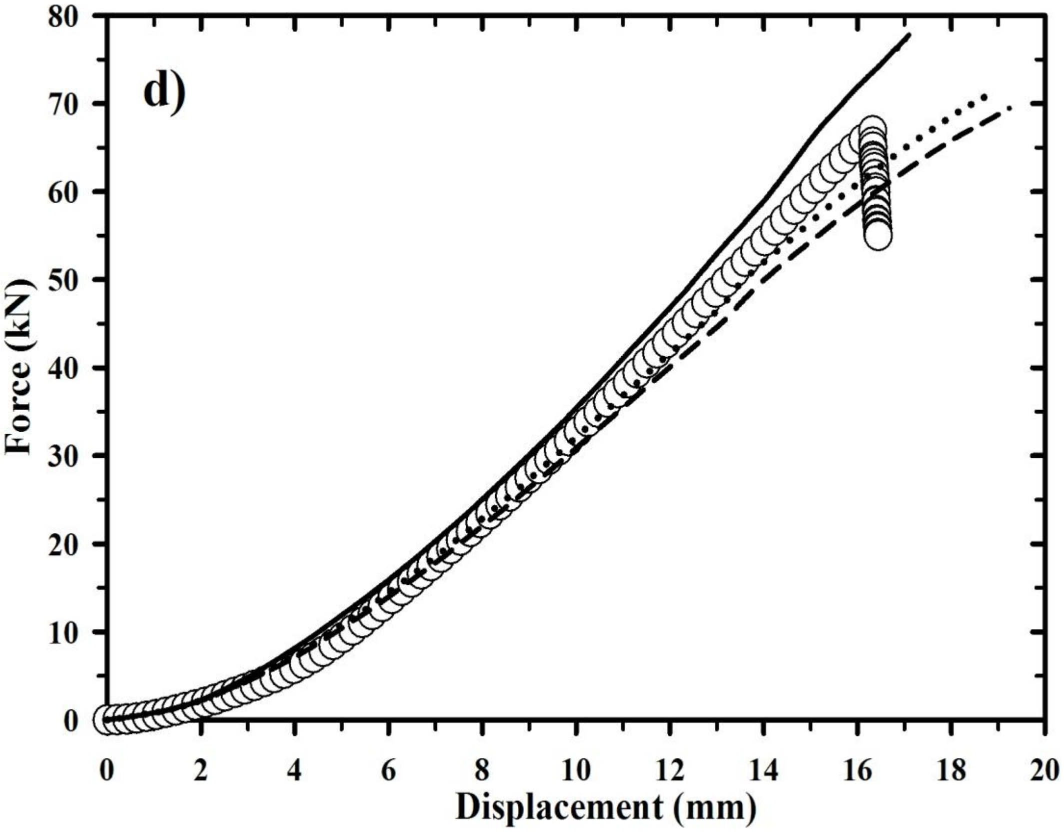

**Figure 6.10** Comparison of force–displacement curves experimentally determined and numerically predicted by different yield functions coupled with the Swift law for the (a) B15, (b) B30, (c) B75 and (d) B115 Nakazima samples

In order to evaluate predictability of the damage curve for crack initiation, each of the Nakazima test was interrupted at the instant when the crack initiation was supposed. The states of crack initiation were characterized by employing the damage curve to the results of the Nakazima test simulations, as shown in Figure 6.8(b) to Figure 6.8(e). The intersections between the stress–strain paths of the critical elements with the respective damage curve were determined. Then, the moments corresponding to these intersection points in the force–displacement curves were identified. Figure 6.11 depicts the critical force levels for the onset of microcrack in each tested sample, which were predicted based on the damage curves and corresponding FE simulations. It could be seen that the determined states of crack initiation of each sample were in good agreement with their following states of instability onset. In the investigated steel, crack formation took place rather early during forming. By the interrupted tests, the samples were deformed until the critical instants. Afterwards, specimens were prepared along sheet thickness from the middle area of the formed Nakazima samples, where the maximum strain was reached. The specimens were examined by SEM to observe existence of emerged microcracks. In addition, SEM images of the middle areas close to the fracture surfaces of each failed sample were taken for comparison. These SEM results described states of plastic instability onset for each corresponding stress condition. The void initiation and void coalescence were apparently distinguished in the SEM images of all the four cases, as illustrated in Figure 6.12 to Figure 6.15. A few and small microcracks were found during the crack initiation states, whereas both amount and size of the microcracks significantly increased at the instability state due to the plastic deformation. It was hereby verified that the determined damage curves regarding crack initiation could fairly predict the crack onset instants in the Nakazima sheet samples of the investigated DP steel under different states of stress. Similar SEM observation of microcracks in interrupted tensile tests was done by Lian et al. [64].

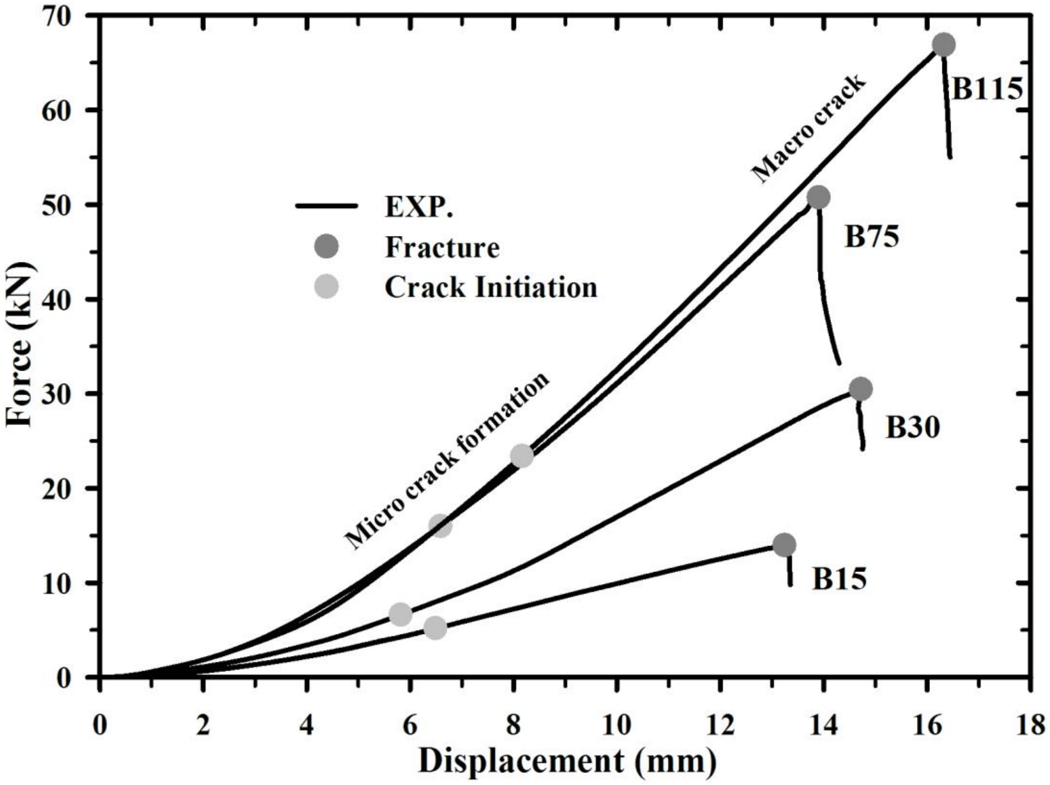

**Figure 6.11** States of crack initiation of deformed Nakazima samples in force – displacement curves identified by the obtained damage curves and FE results

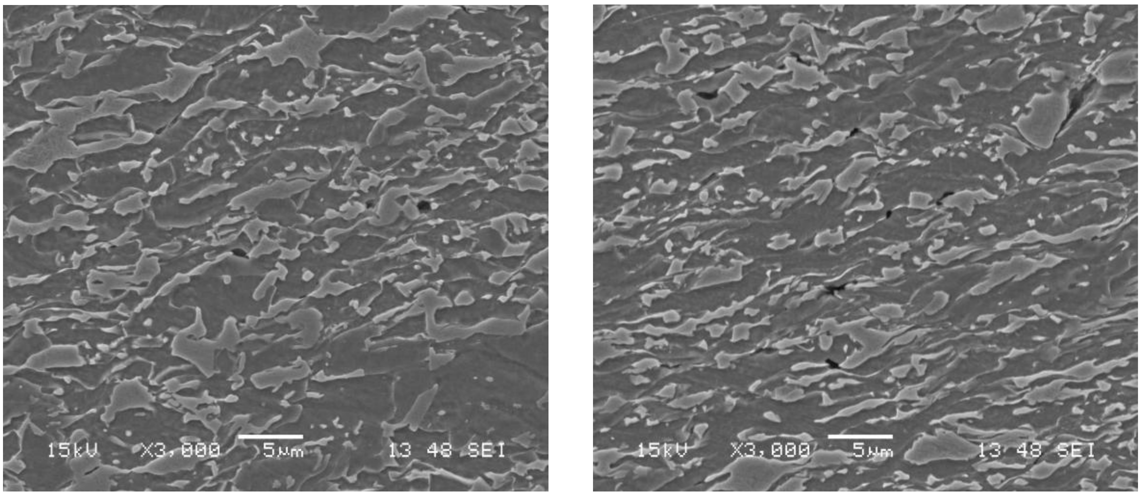

(a) (b)

**Figure 6.12** SEM images of the middle area of the Nakazima sample B15 (a) at the crack initiation state and (b) at the instability state

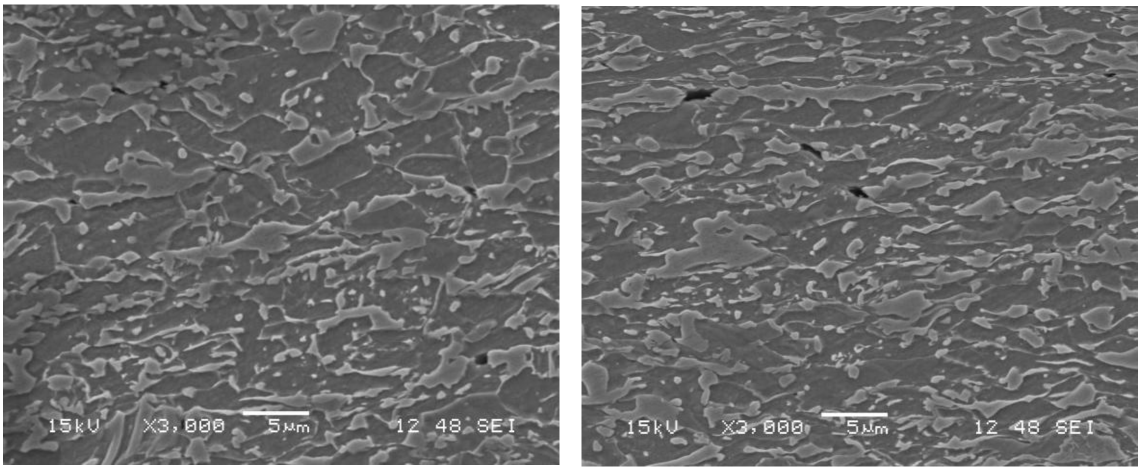

(a) (b)

**Figure 6.13** SEM images of the middle area of the Nakazima sample B30 (a) at the crack initiation state and (b) at the instability state

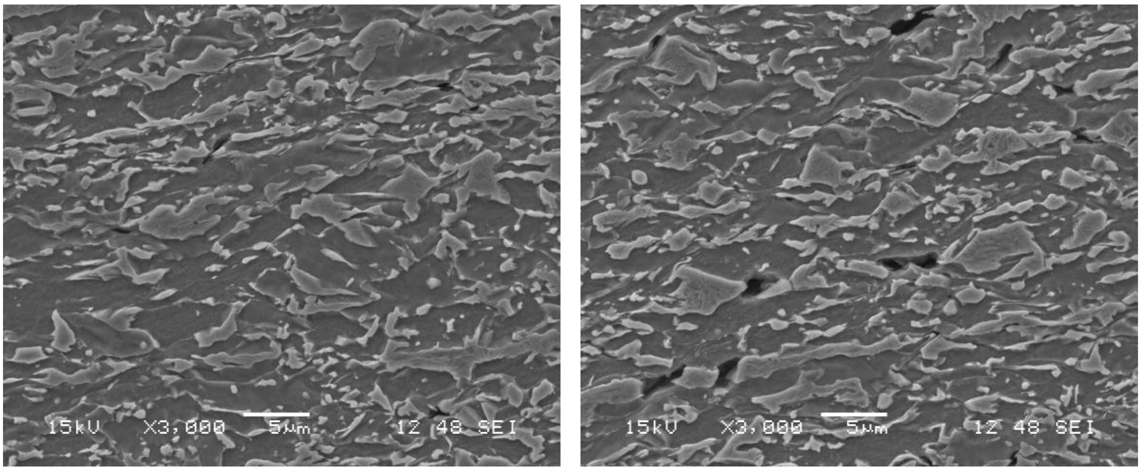

(a) (b)

**Figure 6.14** SEM images of the middle area of the Nakazima sample B75 (a) at the crack initiation state and (b) at the instability state

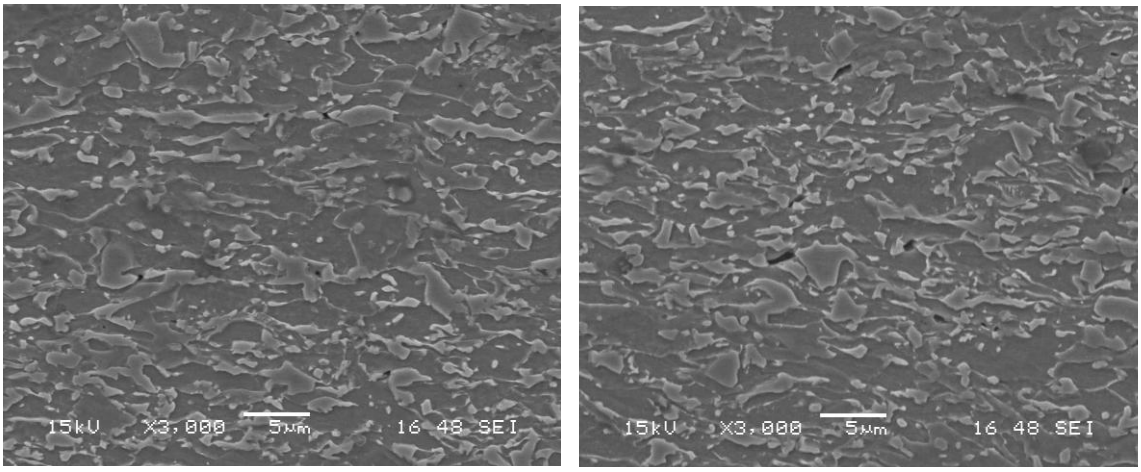

(a) (b)

**Figure 6.15** SEM images of the middle area of the Nakazima sample B115 (a) at the crack initiation state and (b) at the instability state

Another set of damage curves was determined based on the results from notched tensile tests and their corresponding FE simulations with different yield criteria at the plastic instability points. Note that instants short before reaching the maximum forces of each tensile sample were considered as the moment of plastic instability or localization. Stress triaxialities and effective strains at the instability points, gathered from their respective FE simulations with the three different yield functions, were plotted to generate damage curves for plastic instability (so–called instability DCs). They were shown and compared with the damage curves for crack initiation (so–called crack initiation DCs) in Figure 6.16(a). An additional instability point under the balanced–biaxial tensile loading with the stress triaxiality value of 0.667 was obtained from the hydraulic bulge test of the investigated DP steel and used for the instability DCs. It should be noticed that the same experiment could not be done for determining crack initiation, since the DCPD technique could not be applied to the biaxial test sample. Thus, critical plastic strain for crack onset state was not evaluated under the biaxial state. Nevertheless, the similar trend of the instability DCs in the biaxial range was presumed for the crack initiation DCs. From Figure 6.16(a), it could be seen that all the instability DCs regarding different yield criteria are definitely higher than the crack initiation DCs at all states of stress. Nevertheless, at the low triaxiality range, the thresholds of crack initiation and plastic instability were nearby to each other. It meant that macroscopic fracture of the steel could occur recently after microcrack onset under such loading condition. Also, the instability and crack initiation DCs based on the Yld2000–2d function are higher than those based on the von Mises and Hill’48 model. The damage curves from the von Mises and Hill’48 criterion exhibited only slight deviations. Some discrepancies were observed among the stress–strain paths of each Nakazima sample predicted by different yield functions, as shown in Fig. 18b–18e and until large plastic deformation in Figure 6.16(b) – Figure 6.16(e). The stress triaxialities in all Nakazima samples gradually increased from forming start and then abruptly reached the constant values describing each governing stress state. The sample B15 exhibited a final steady stress triaxiality of about 3.5, which was close to that of the uniaxial tension. The sample B30 showed a stress triaxiality of about 0.5, whereas both B75 and B115 samples tended to present a stress triaxiality of 0.667 close to the biaxial stress state. The stress–strain paths of all 4 samples intersected with the crack initiation DCs and instability DCs, as seen in Figure 6.16(b) – Figure 6.16(e), at which occurred crack initiation and plastic instability of the corresponding Nakazima samples were predicted during forming.

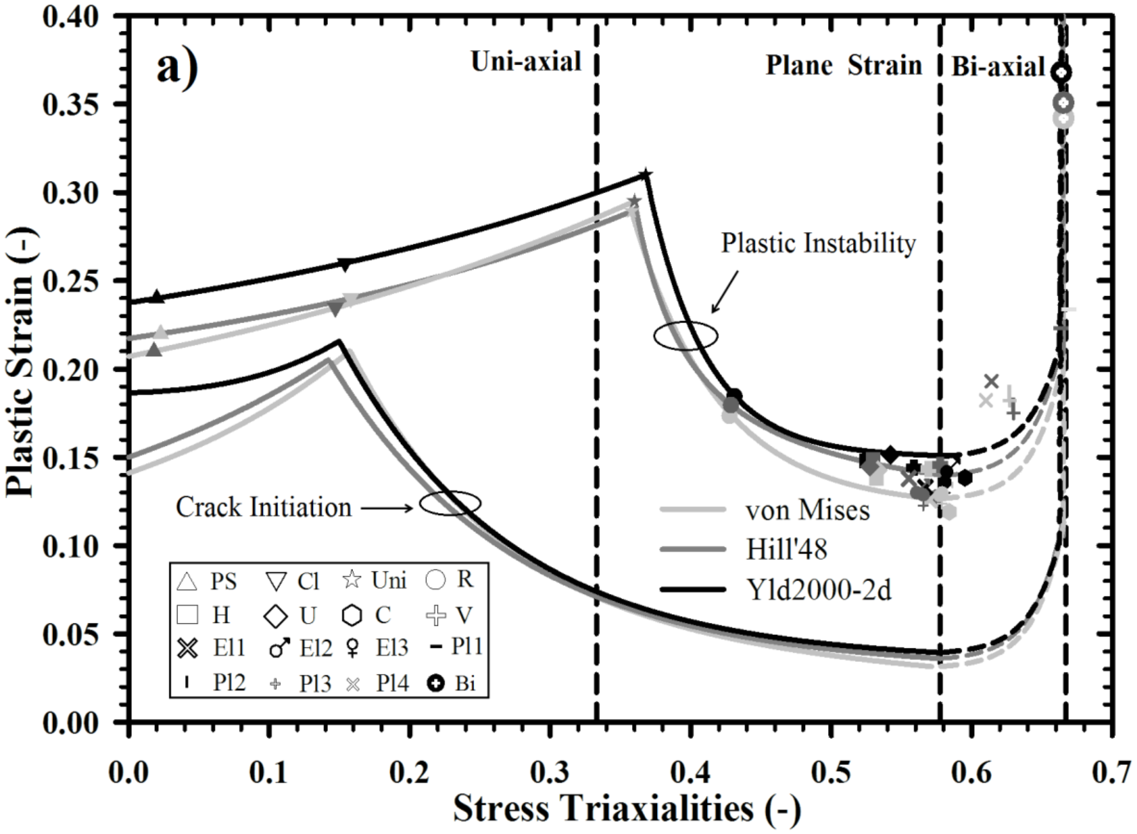
a)
Uni-axial
Plane Strain
Bi-axial
Plastic Instability
Crack Initiation
von Mises
Hill'48
Yld2000-2d
△ PS
▽ Cl
☆ Uni
○ R
□ H
◇ U
⬡ C
✚ V
✖ El1
♂ El2
♀ El3
- Pl1
ı Pl2
+ Pl3
× Pl4
⊕ Bi
Plastic Strain (-)
0.00
0.05
0.10
0.15
0.20
0.25
0.30
0.35
0.40
Stress Triaxialities (-)
0.0
0.1
0.2
0.3
0.4
0.5
0.6
0.7

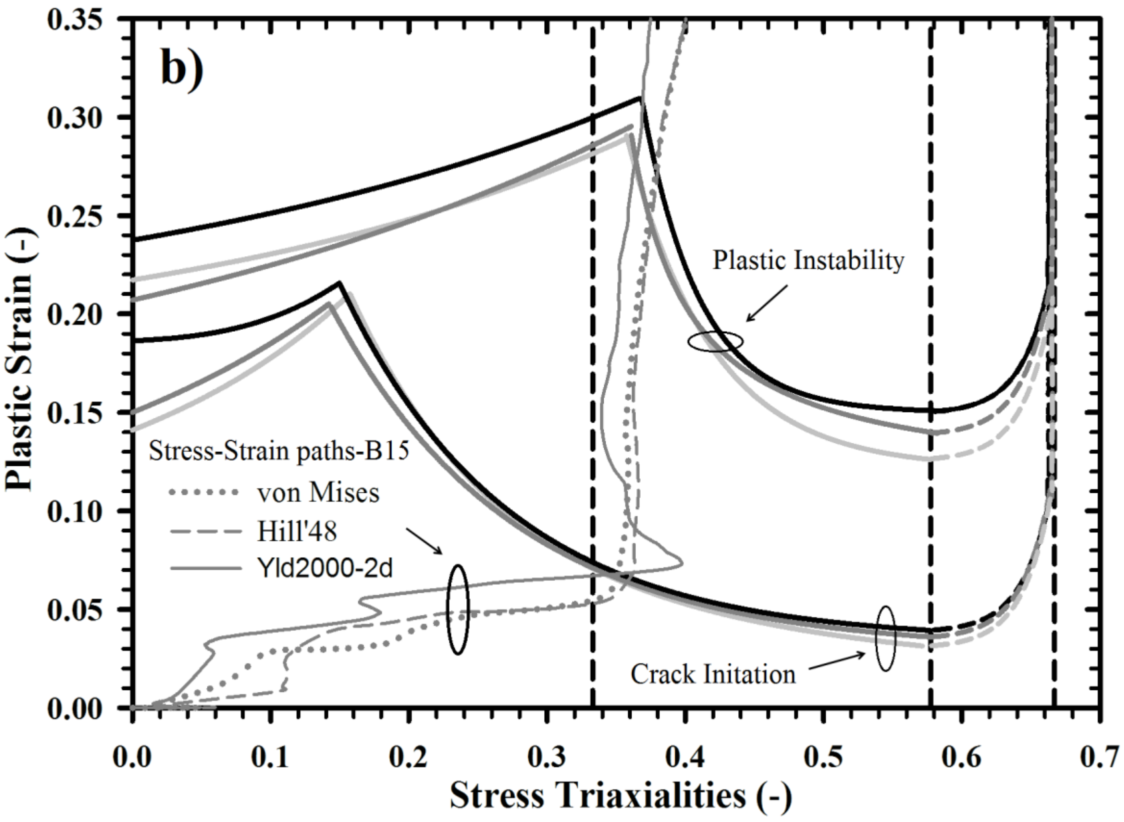
b)
Plastic Instability
Stress-Strain paths-B15
von Mises
Hill'48
Yld2000-2d
Crack Initation
Plastic Strain (-)
0.00
0.05
0.10
0.15
0.20
0.25
0.30
0.35
Stress Triaxialities (-)
0.0
0.1
0.2
0.3
0.4
0.5
0.6
0.7

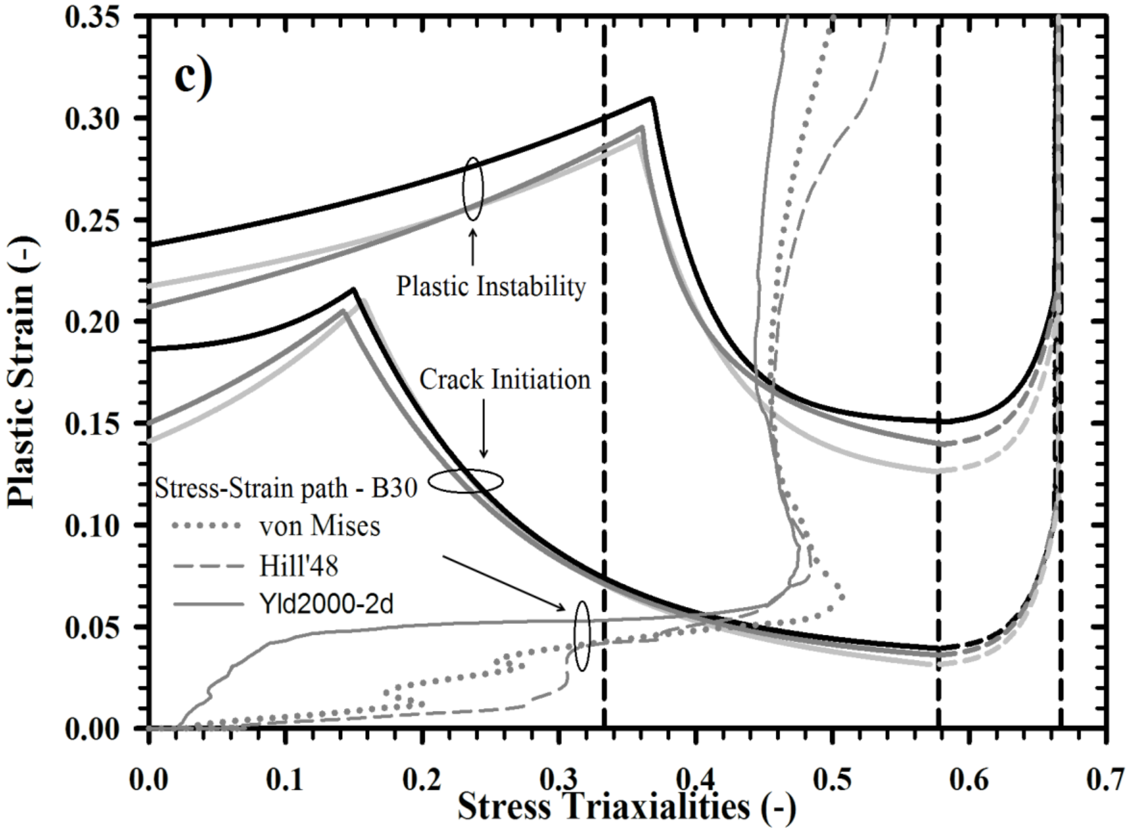
c)
Plastic Strain (-)
Stress Triaxialities (-)
0.35
0.30
0.25
0.20
0.15
0.10
0.05
0.00
0.0
0.1
0.2
0.3
0.4
0.5
0.6
0.7
Plastic Instability
Crack Initiation
Stress-Strain path - B30
von Mises
Hill'48
Yld2000-2d

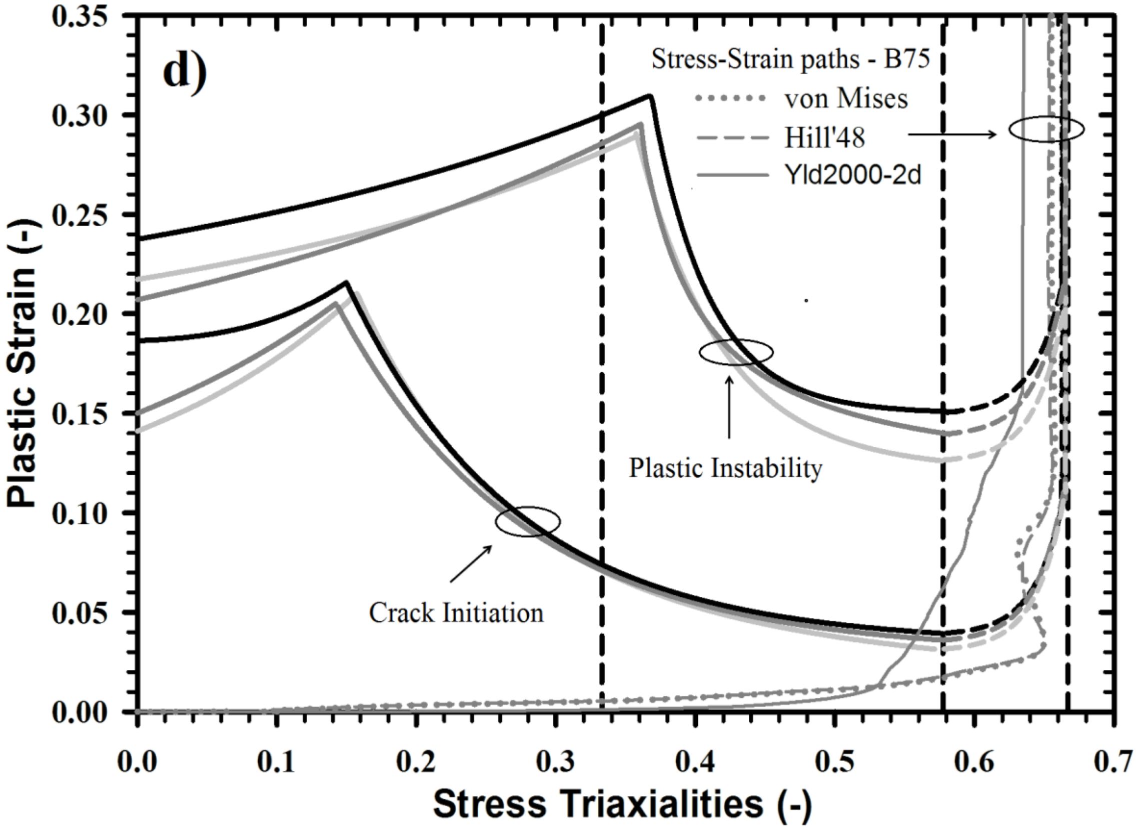
d)
Plastic Strain (-)
Stress Triaxialities (-)
0.35
0.30
0.25
0.20
0.15
0.10
0.05
0.00
0.0
0.1
0.2
0.3
0.4
0.5
0.6
0.7
Stress-Strain paths - B75
von Mises
Hill'48
Yld2000-2d
Plastic Instability
Crack Initiation

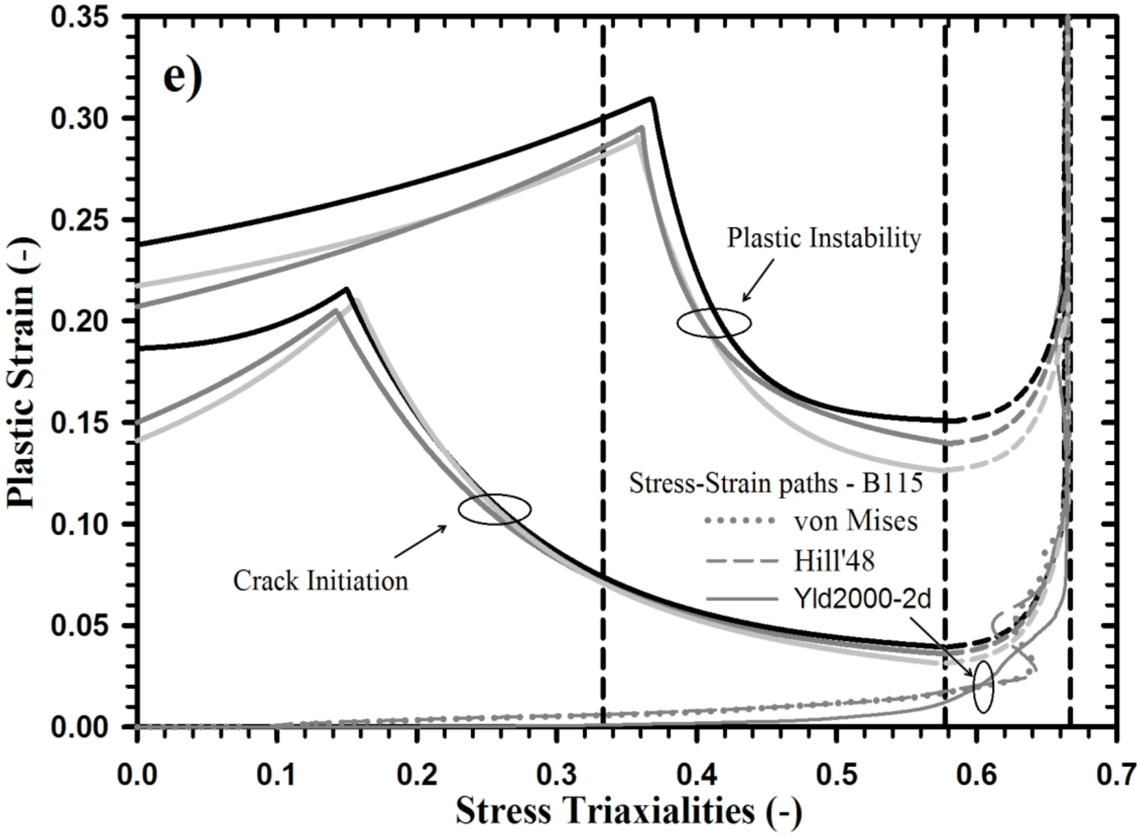

**Figure 6.16** (a) Determined damage curves for crack initiation and plastic instability using different yield criteria and calculated stress–strain paths from (b) B15, (c) B30, (d) B75 and (e) B115 deformed Nakazima samples based on different yield criteria compared to the damage curves

Furthermore, calculated dome heights of the deformed Nakazima samples were determined for the moment of crack initiation and localized necking by means of the crack initiation and instability DCs, respectively, as illustrated in Figure 6.17. Obviously, the DCs based on different yield models provided somewhat varying dome heights at both crack initiation and plastic instability states. The predicted dome heights by using the instability DCs were slightly lower than the experimental measured dome heights for all samples. The instability DCs described final failures of each Nakazima samples at a bit earlier state. However, it should be acceptably applied to formability evaluation of sheet metal forming for the JAC780Y steel.

### 6.3.2 Application to an industrial part

To further verify the applicability of the obtained damage curves for crack initiation and plastic instability, an industrial part stamping of the investigated DP steel grade JAC780Y were performed experimentally and numerically. The part was pressed until material failed on purpose, as shown in Figure 6.18. Four critical areas (P1, P2, P3 and P4) were identified and subject to this investigation. Stress–strain paths of the areas P1 and P2 on the stamped part were calculated by FE simulations coupled with different yield criteria.

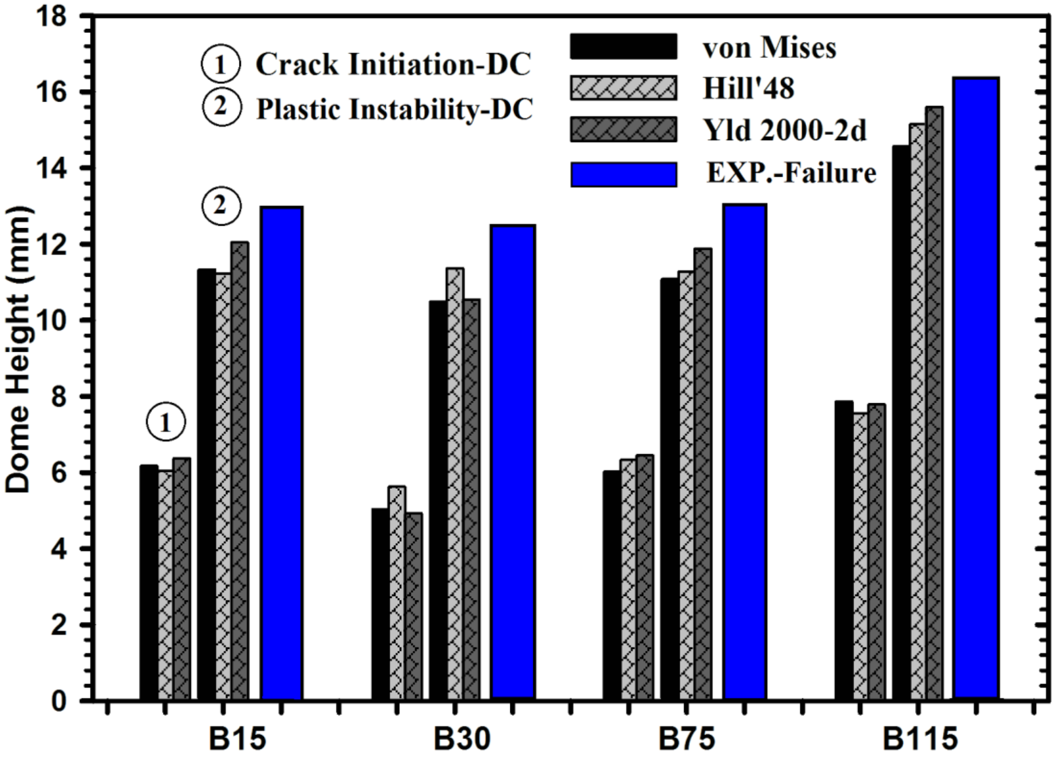

**Figure 6.17** Predicted dome heights of formed Nakazima samples at the moment of crack initiation and plastic instability calculated by means of the damage curves based on different yield criteria

The simulations were performed until the same punch stroke as in the experiments. It was found that the determined stress–strain paths strongly depended on the yield criterion and observed locations. The stress–strain paths from the critical areas of the complex part showed greatly discontinuous behavior, in contrast to those of the Nakazima samples. The calculated paths of the areas P1 and P2 intersected the crack initiation DCs and plastic instability DCs successively, as seen in Figure 6.19(a) and Figure 6.19(b). It meant that fracture was predicted at these areas, which was in accordance with the experimental results. On the other hand, the area P3 and P4 located in the pressed part were highly deformed, but no fracture was observed. Correspondingly, their stress–strain paths, depicted in Fig. 6.19(c) and Figure6.19(d), crossed over the crack initiation DCs, but not yet reached the instability DCs. Evidently, these instability DCs can be applied successfully to formability prediction of industrial sheet metal forming process. Additionally, microcrack formation was predicted in the formed industrial part at all critical areas. However, the states of crack initiation in different locations varied with respect to the local stress–strain condition. In addition, it was found that the stress–strain paths calculated using different yield criteria for the area P1 and P4 slightly deviated, where the part was locally loaded under high stress triaxiality condition. In contrast, the stress–strain paths for the areas P2 and P3 showed large discrepancies, where the part was governed by low triaxiality value and failure eventually occurred due to shear fracture.

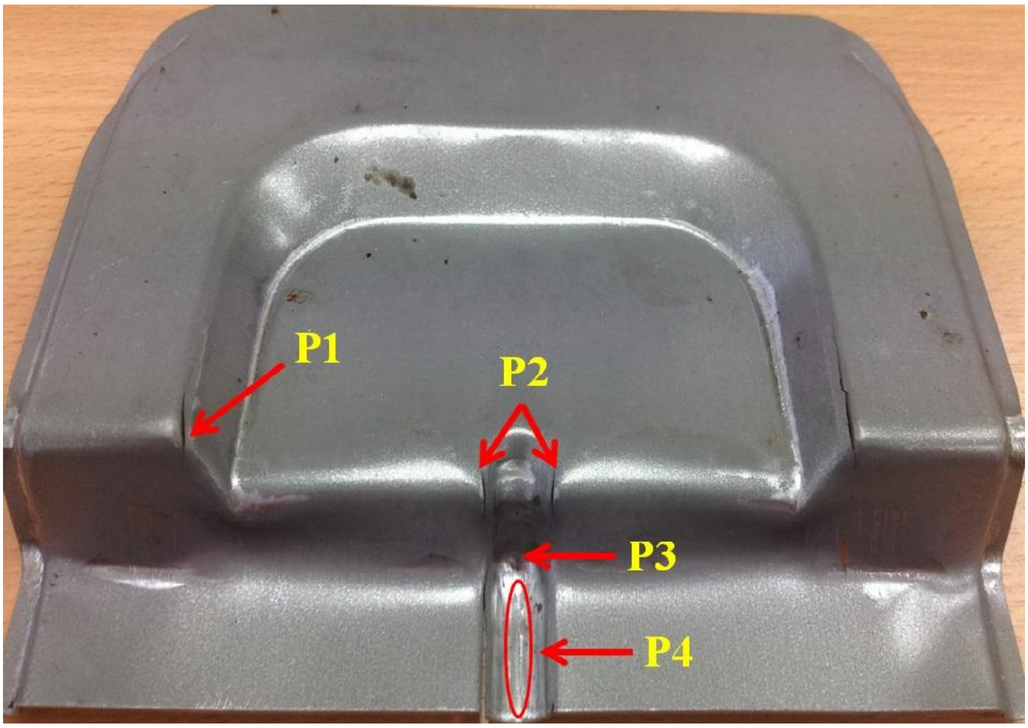

**Figure 6.18** Stamped industrial part at failure with indicated fracture areas

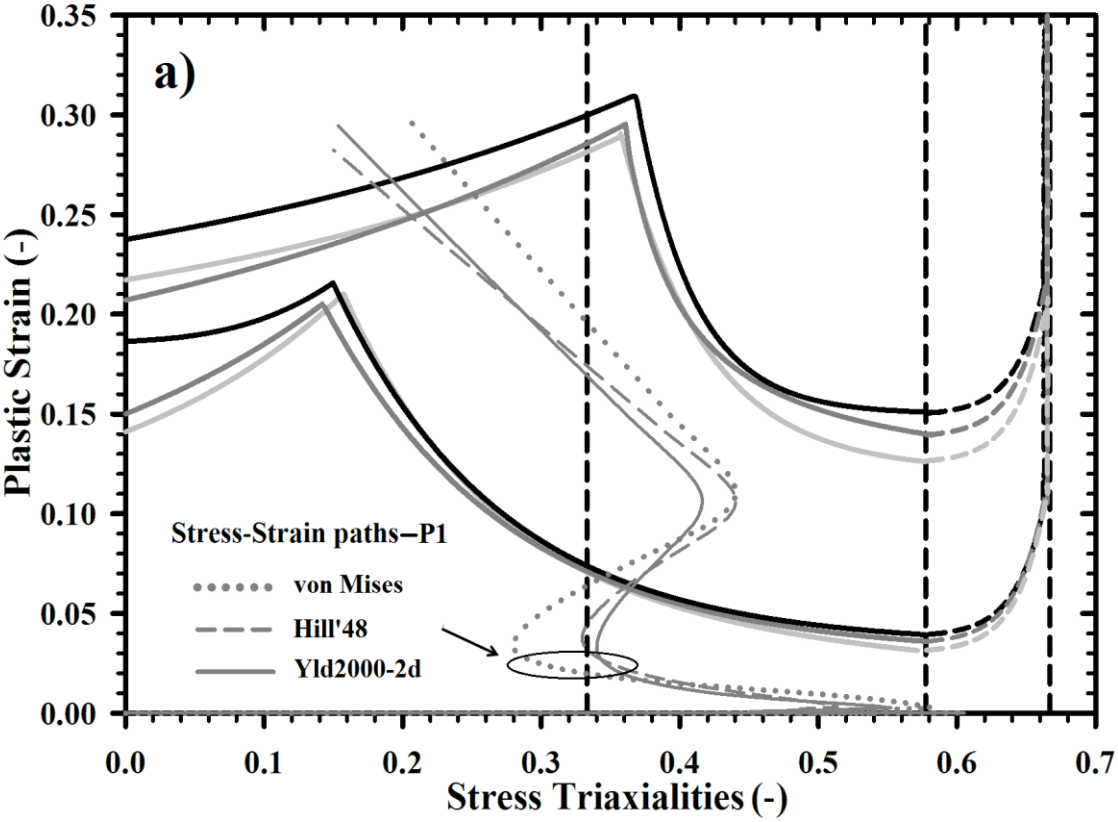

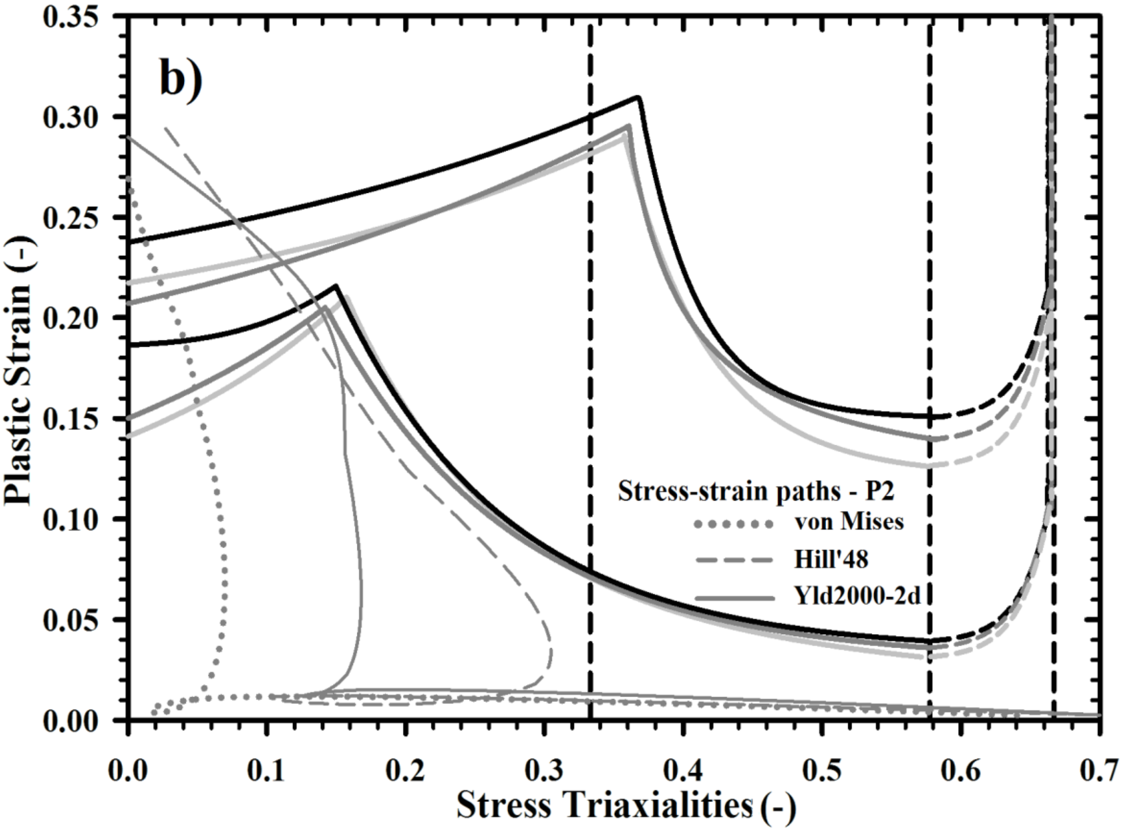
b)
Plastic Strain (-)
Stress Triaxialities (-)
0.00
0.05
0.10
0.15
0.20
0.25
0.30
0.35
0.0
0.1
0.2
0.3
0.4
0.5
0.6
0.7
Stress-strain paths - P2
von Mises
Hill'48
Yld2000-2d

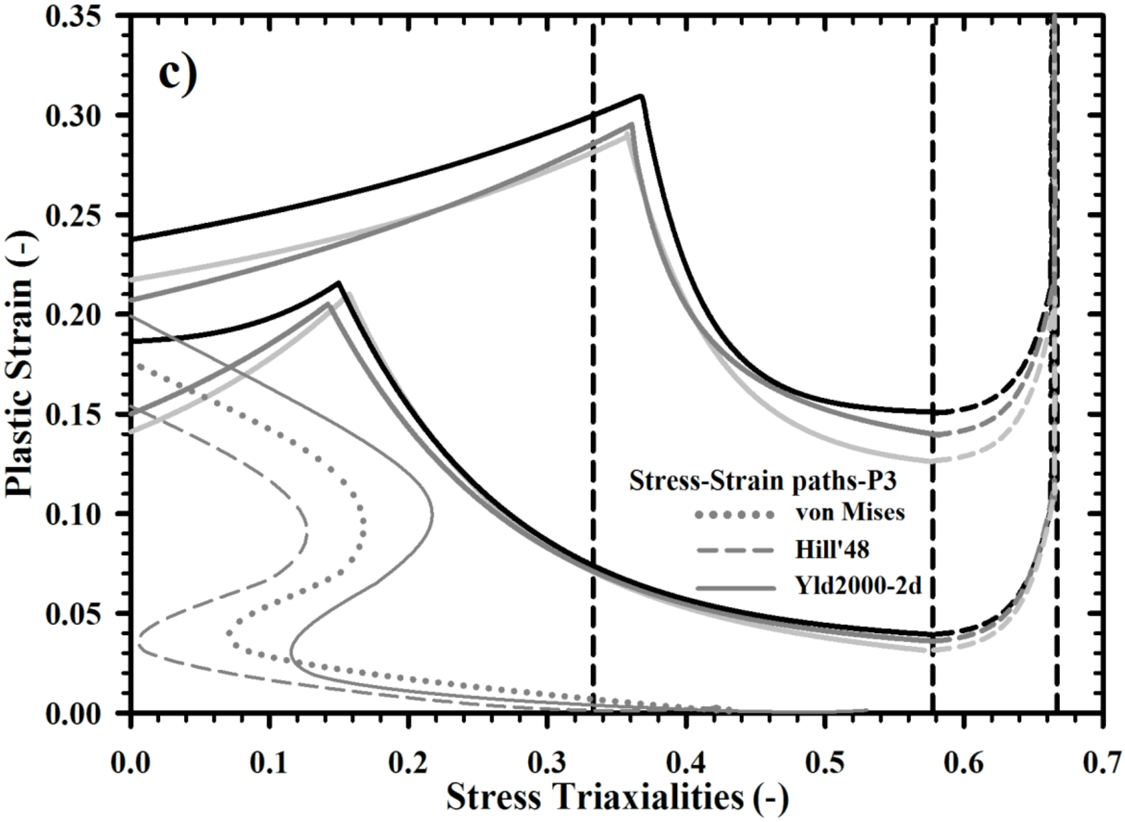
c)
Plastic Strain (-)
Stress Triaxialities (-)
0.00
0.05
0.10
0.15
0.20
0.25
0.30
0.35
0.0
0.1
0.2
0.3
0.4
0.5
0.6
0.7
Stress-Strain paths-P3
von Mises
Hill'48
Yld2000-2d

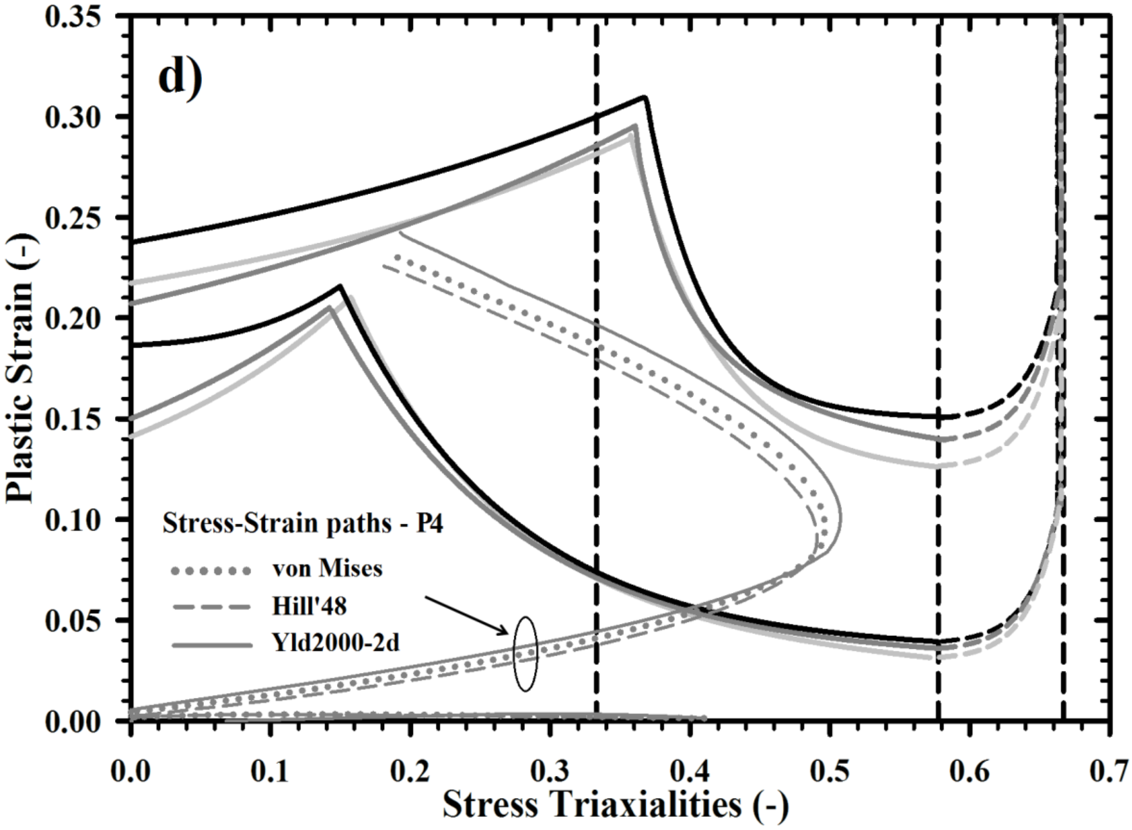

**Figure 6.19** Stress–strain paths from the areas (a) P1, (b) P2, (c) P3 and (d) P4 of the industrial part calculated using different yield criteria in comparison with the damage curves

### 6.3.3 Application of FLDs based on damage curve

The crack initiation DCs and plastic instability DCs coupled with various yield criteria were developed by the hybrid approach using experimental and numerical analysis, as demonstrated in Figure 6.8(a) and Figure 6.16(a). In this study, the damage curves (DCs) in stress triaxiality and effective plastic strain domain were transformed to forming limit curves (FLCs) in space of principle strains by using Equations (2.24) – (2.26). Figure 6.20 illustrates the damage curves in three principal states of stress (pure shear, uniaxial and biaxial). The correspondingly obtained forming limit curves were given in Figure 6.21. Obviously, the FLCs based on the damage curves resembled the shape of conventional FLCs with additional range of strain on the far left hand side, generally governed by shear fracture mode.

Basically, the crack initiation DCs and instability DCs consisted of three branches in the space of effective plastic strain and stress triaxiality, as shown in Fig. 30. The first branch corresponded to the stress states between biaxial tension ($\eta = 0.667$) and plane strain ($\eta = 0.577$). The second branch covered the range from plane strain ($\eta = 0.577$) to uniaxial tension ($\eta = 0.33$). The third branch extended from uniaxial tension ($\eta = 0.33$) to pure shear ($\eta = 0$). The three branches could be uniquely transformed to the principal strain space. The resulting strain locus for crack initiation and plastic instability are referred to as the crack initiation forming limit curve (CIFLC) and plastic instability forming limit curve (IFLC), as demonstrated in Figure 6.21. Similar to the damage curve, the first branch corresponded to the strain states between equi–biaxial tension ($\varphi_1 = \varphi_2$) and plane strain ($\varphi_2 = 0$). The second branch regarded the range from plane strain ($\varphi_2 = 0$) to uniaxial tension ($\varphi_1 = -2\varphi_2$). The last branch is applicable to strain state from uniaxial tension ($\varphi_1 = -2\varphi_2$) to pure shear ($\varphi_1 = -\varphi_2$). The determined crack initiation FLCs based on various yield functions were very similar in all strain states. Small deviations were observed in the range between uniaxial tension and pure shear load, in which the Yld2000–2d model provided somewhat higher predicted limit strains. The calculated instability FLCs by various yield functions exhibited small discrepancies at all states of strain, since plastic deformation became larger so that the yield function affected the limit strains. The obtained crack initiation and instability FLCs had similar characteristics as the results shown in Li et al. [109].

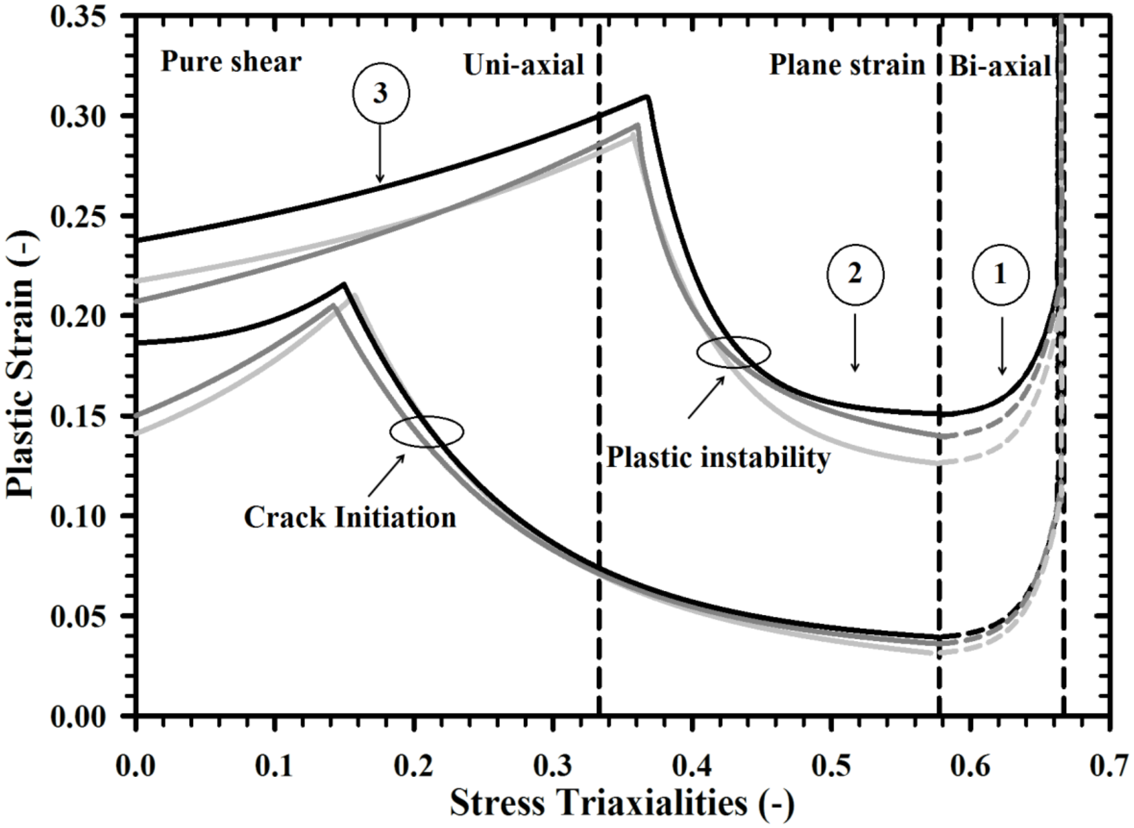

**Figure 6.20** Illustrated DCs represented in plane stress triaxialities and plastic strain

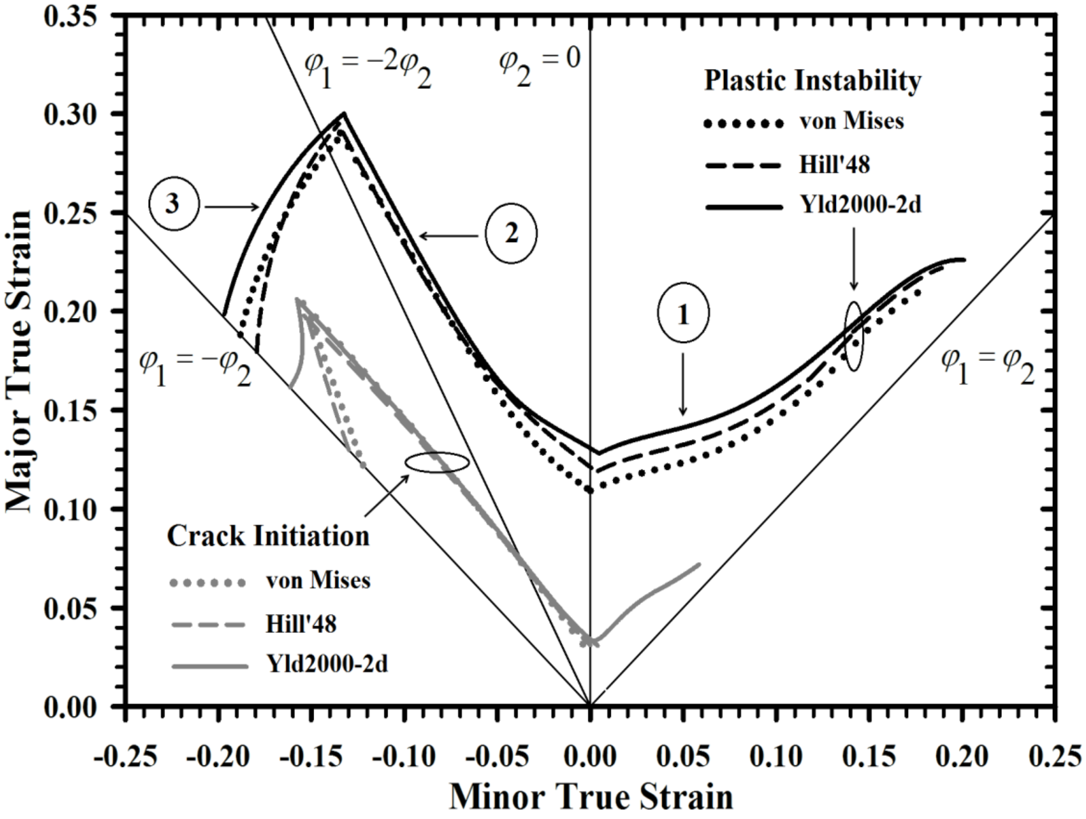

**Figure 6.21** Determined forming limit curves based on crack initiation and instability DCs using different yield criteria

Figure 6.21 represents the complete obtained FLCs regarding crack initiation and plastic instability. It should be noted that the conventional FLC determined by experimental Nakazima test, seen as EXP.–JAC780Y in Figure 6.22, or so–called Nakazima based FLC was commonly used for formability evaluation of sheet metals in part making industries. It was reported that the Nakazima based FLC could not accurately describe material failure due to shear fracture, which was the typical failure mode of complex AHS steel part [109]. These introduced damage curve (DC) based FLCs offered a clue for predicting such shear fractures in sheet metal parts. Generally, there were two different approaches for describing ductile fracture of metal, as expressed in Li and Wierzbicki [110]. For the first approach, fracture was modeled as a process of damage accumulation within the continuum, which meant that the constitutive model and fracture model were coupled. For the second approach, fracture was considered as a sudden event when the stress and strain state of the undamaged continuum reached a critical level. The former type was referred to as “coupled” fracture modeling and the latter as “uncoupled” fracture modeling. Both of them showed advantages and disadvantages. Note that the method used in this study was the “uncoupled” approach. Elastic–plastic behavior of the examined steel in the forming tests was only described by the Swift hardening law and yield models, in which no fracture model was incorporated. Nevertheless, anisotropy behavior of the material was taken into account. Meanwhile, the damage criteria and corresponding FLCs have been developed based on crack initiation and plastic instability. In Figure 6.22, the FLCs based on the plastic instability DCs (IFLCs) are located under the Nakazima based FLC. It meant that the instability FLCs could predict the formability limits of material sooner than the conventional one, therefore the DC based FLCs were more conservative. Especially, in the domain between uniaxial tension and pure shear, the limit strains of the DC based FLCs were much lower than those of the conventional FLC. Generally, the FLCs based on crack initiation (CIFLCs) were lowest of all the FLCs, since they predicted damage at the microscopic level. The prediction of microcrack onset is necessary for AHS steels when utilized in automotive parts under cyclic loading, whereby fatigue crack is supposed.

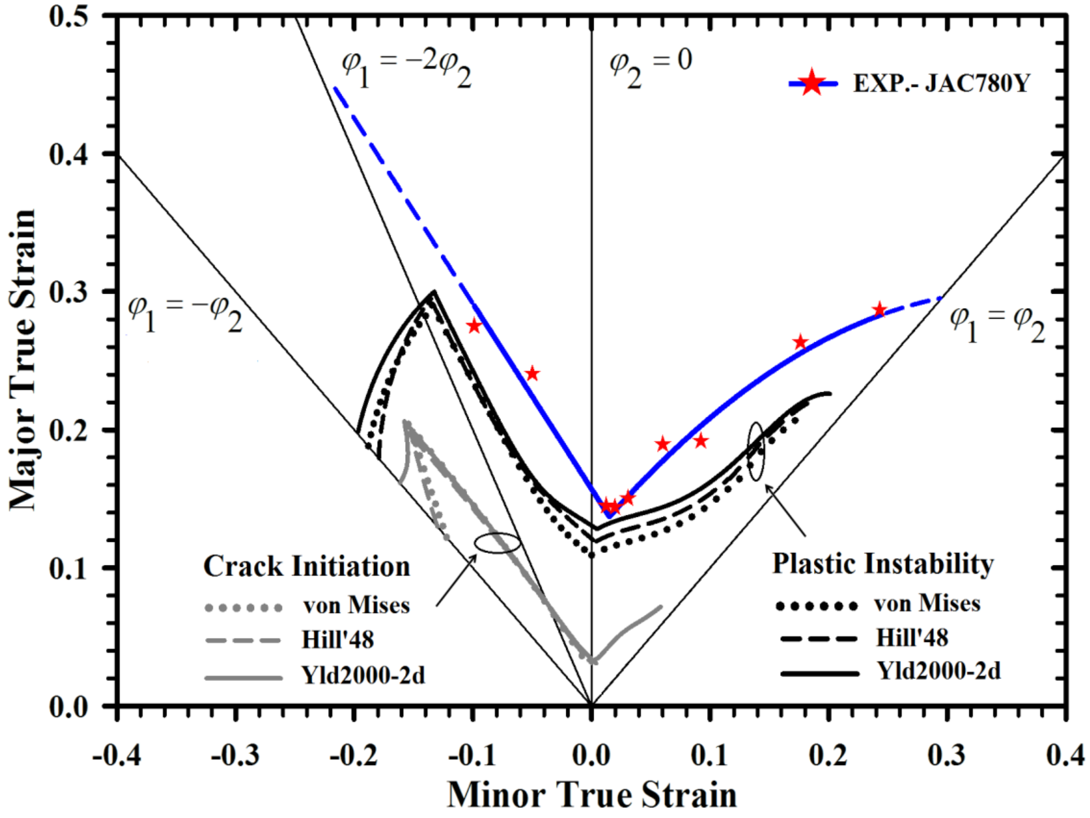

**Figure 6.22** Comparison between FLCs based on Nakazima test and FLCs calculated by the crack initiation and instability DCs for the investigated DP steel

Also, applicability of the determined DC based FLCs was proved by the four used Nakazima samples and the industrial stamping part. As mentioned, the force–displacement curves from the stretch–forming experiments and FE simulations were compared first in order to verify the simulation results and to identify the point of time when failure took place during the experiments. Then, from the FE simulations, major and minor principal strains were obtained from the identified crack initiating elements up to the instants of failure or maximum load in the experiments. The principal strain paths extracted from the FE simulations applying three different yield criteria were plotted together with the instability and Nakazima based FLDs for the JAC780Y steel in Figure 6.23. The strain paths of all Nakazima samples exhibited continuous linear characteristics until fracture in different ranges of state of strain, similar to those stress–strain paths in Figure 6.16(b) – Figure 6.16(e). It was found that the failures of all deformed Nakazima samples occurred very close to the DC based FLCs, but somewhat earlier than the limit strains from the conventional FLC. It meant that the instability DC based FLC could more precisely describe plastic instability state of the investigated DP steel than the Nakazima based FLC. In other words, formability prediction of the determined DC based FLDs was more satisfactory than that of the conventional FLD.

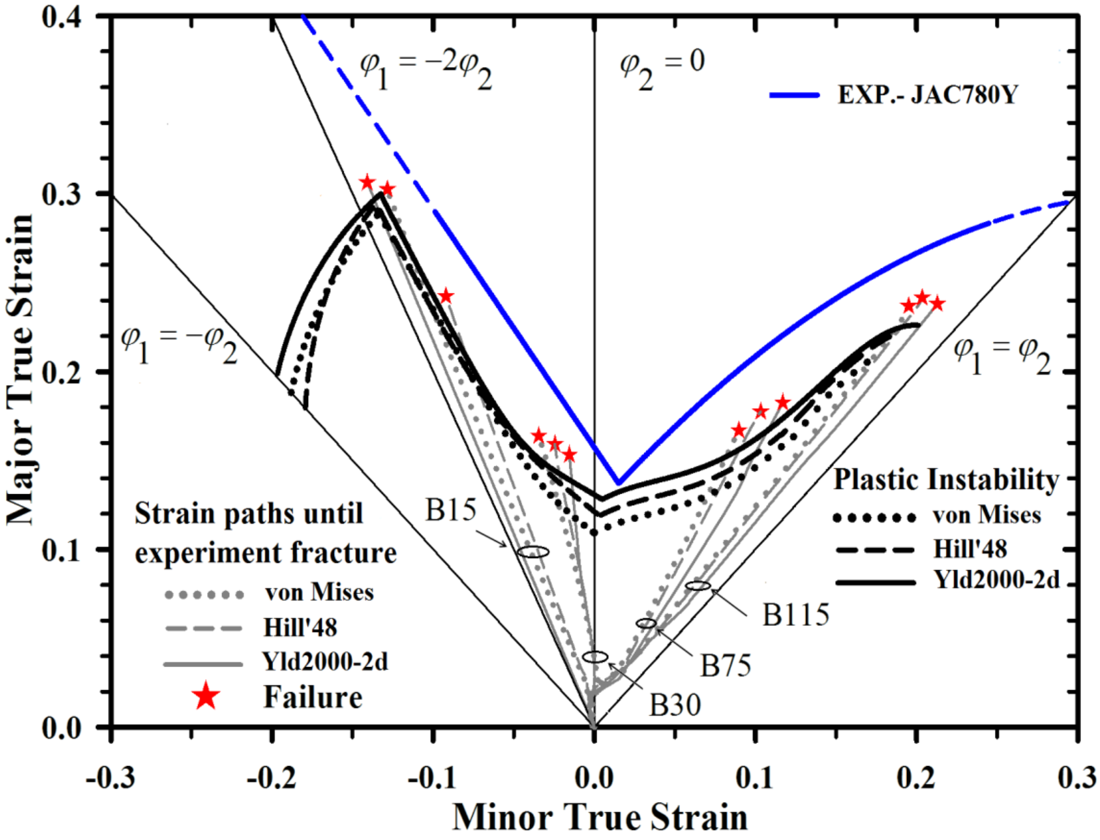

**Figure 6.23** Strain paths of the critical elements in the Nakazima stretching test calculated by FE simulations until the experimental failure using different yield criteria in comparison with the instability DC based FLDs

Additionally, the instability DC based FLC calculated using the Yld2000–2d model was higher than the ones regarding the Hill’48 and von Mises criterion, respectively. Some discrepancies were observed among the strain paths of each Nakazima sample predicted by different yield criteria. Both slopes and failure strains of the strain paths were different. The sample B15 illustrated major and minor principle strains, which closed to the uniaxial strain state. The sample B30 located close to the plane strain and the sample B115 was nearest with the biaxial strain state. The strain paths of all four samples crossed and slightly overestimated the instability DC based FLCs, but never met the Nakazima based FLC. Obviously, the instability DC based FLCs can predict the early failure before localized necking of such AHS steels, successfully.

By the same manner as aforementioned, applicability of the DCs based FLCs obtained, FE simulations of the industrial part stamping were performed and major and minor principle strain paths until the state of experimental fracture of those four critical areas were numerically evaluated using different yield functions. The strain paths of area P1 and P2 were plotted on the instability DC based FLC and conventional FLC of the examined steel, as shown in Fig. 34a and 34b. The strain path of the area P1 located between the range of uniaxial tension and plane strain, whereas the strain path of the area P2 was between the range of deep drawing or pure shear and uniaxial tension. The strain paths of both areas crossed over the instability DC based FLCs, but not yet passed the Nakazima based FLC. It meant that fracture occurred in the area P1 and P2 could be accurately described, in particular, the quasi–shear fracture mode in the area P2 by the instability DC based FLCs. In contrast, the area P3 and P4 presented in highly deformed areas, as seen in Fig. 28, but no fracture was definitely observed. Accordingly, the strain paths of the area P3 and P4 until experimental fractures determined using different yield criteria, as demonstrated in Fig. 34c and 34d, respectively, terminated just below the instability DC based FLC but not yet reached the Nakazima based FLC. The results were in agreement with those predictions in Figure 6.19(c) and 6.19(d), since the stress–strain paths of both areas intersected over the crack initiation DCs but never met the instability DCs. It meant that microcrack initiation should already arise in the area P3 and P4, but macroscopic failure or plastic instability was still not occurred.

There are some deviations between the strain paths in both characteristic and fracture strain of each area predicted by different yield criteria. For the areas P1, P3 and P4, the strain paths from various yield models slightly deviated, but for the area P2 the predicted strain path based on the Yld2000-2d model much differed from the other ones. It seemed that the calculated stress and strain responses under shear loading were noticeably affected by the applied yield functions rather than those under other loading conditions. The area P2 particularly demonstrated the use of shear fracture prediction capability of the DCs based FLCs over the conventional Nakazima based FLCs, definitely. It can be drawn here that the DCs based FLCs are a good conservative predictive tool with additional capability to predict shear fracture failure mode. They are suitable for applications in industrial environment.

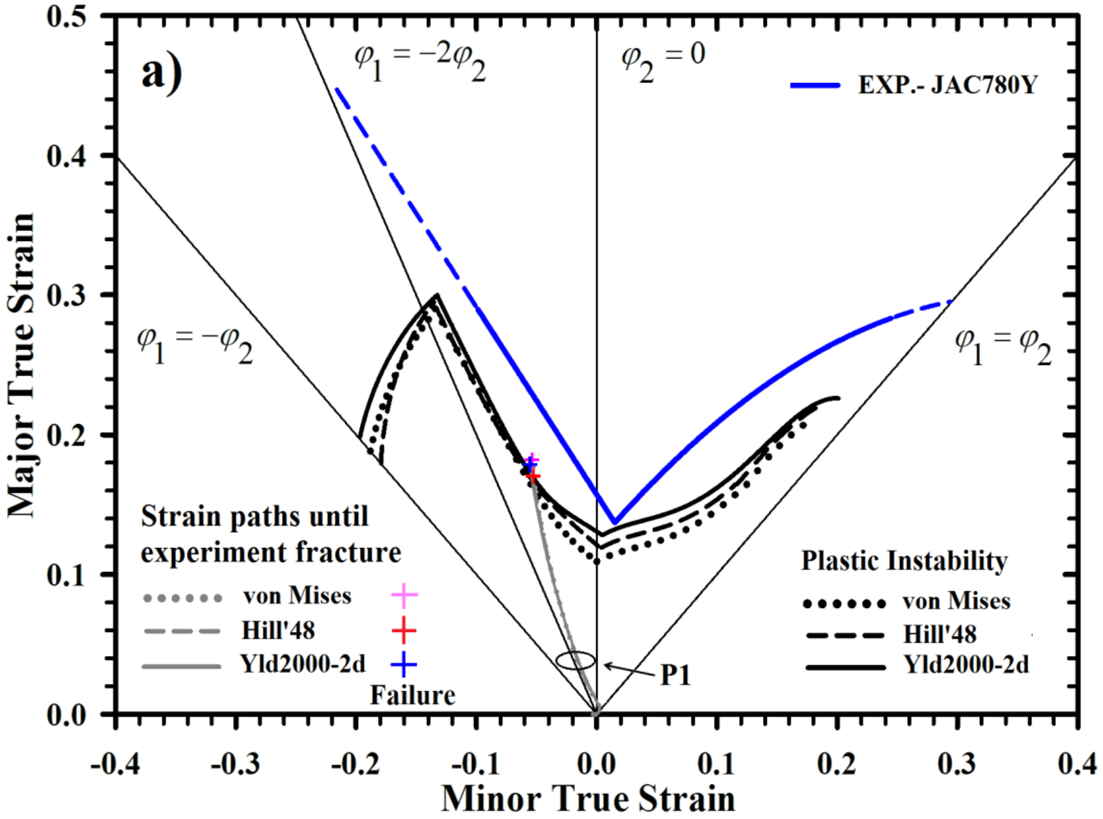

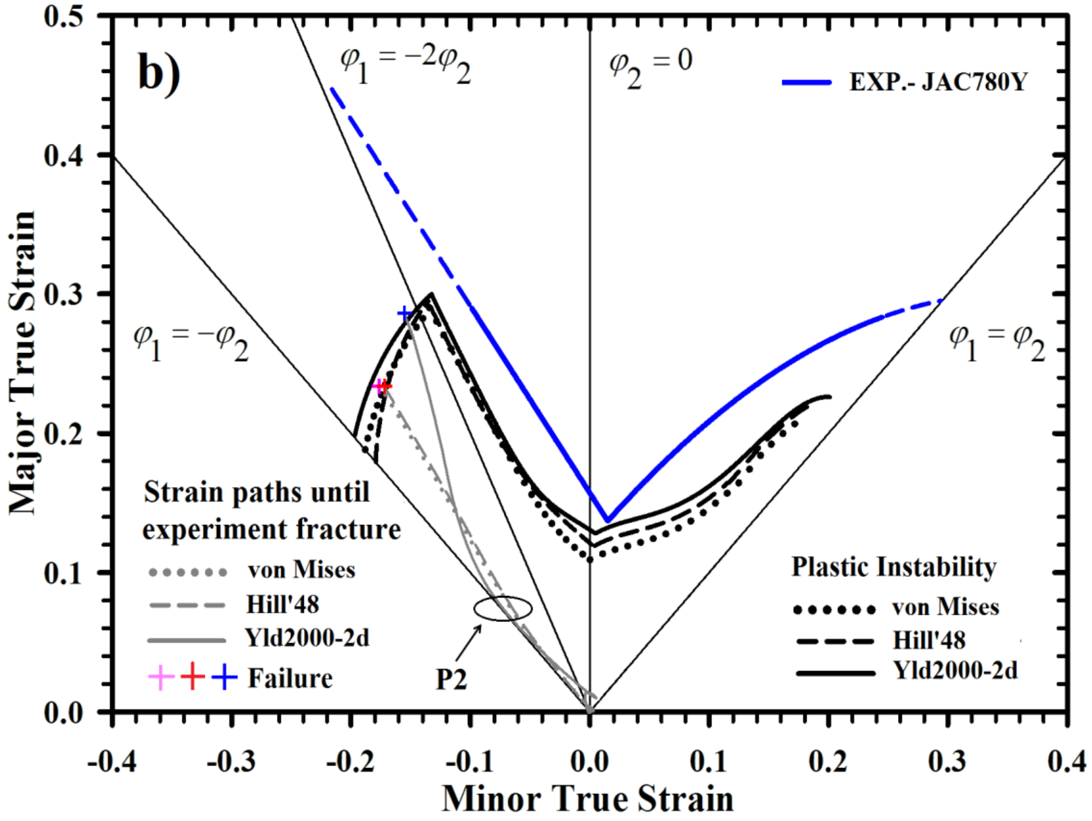
b)
φ1 = −2φ2
φ2 = 0
φ1 = −φ2
φ1 = φ2
EXP.- JAC780Y
Strain paths until experiment fracture
von Mises
Hill'48
Yld2000-2d
Failure
P2
Plastic Instability
von Mises
Hill'48
Yld2000-2d
Major True Strain
0.0
0.1
0.2
0.3
0.4
0.5
Minor True Strain
-0.4
-0.3
-0.2
-0.1
0.0
0.1
0.2
0.3
0.4

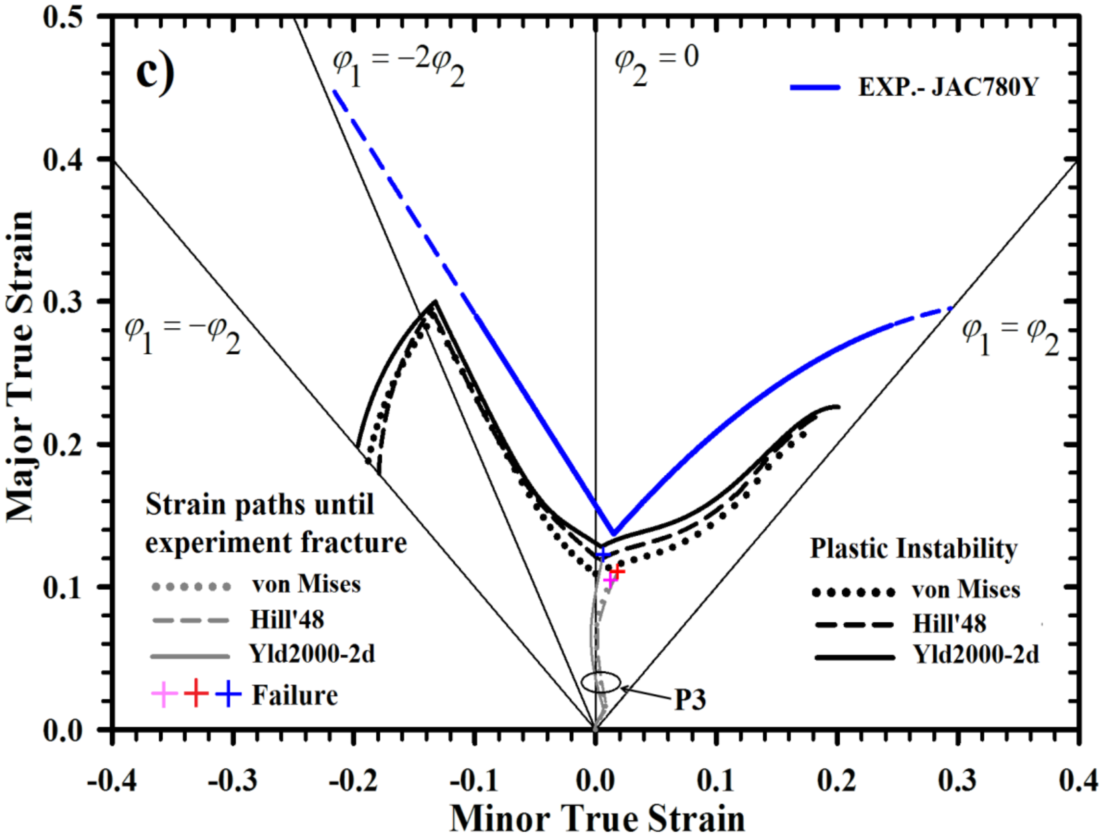
c)
φ1 = −2φ2
φ2 = 0
φ1 = −φ2
φ1 = φ2
EXP.- JAC780Y
Strain paths until experiment fracture
von Mises
Hill'48
Yld2000-2d
Failure
P3
Plastic Instability
von Mises
Hill'48
Yld2000-2d
Major True Strain
0.0
0.1
0.2
0.3
0.4
0.5
Minor True Strain
-0.4
-0.3
-0.2
-0.1
0.0
0.1
0.2
0.3
0.4

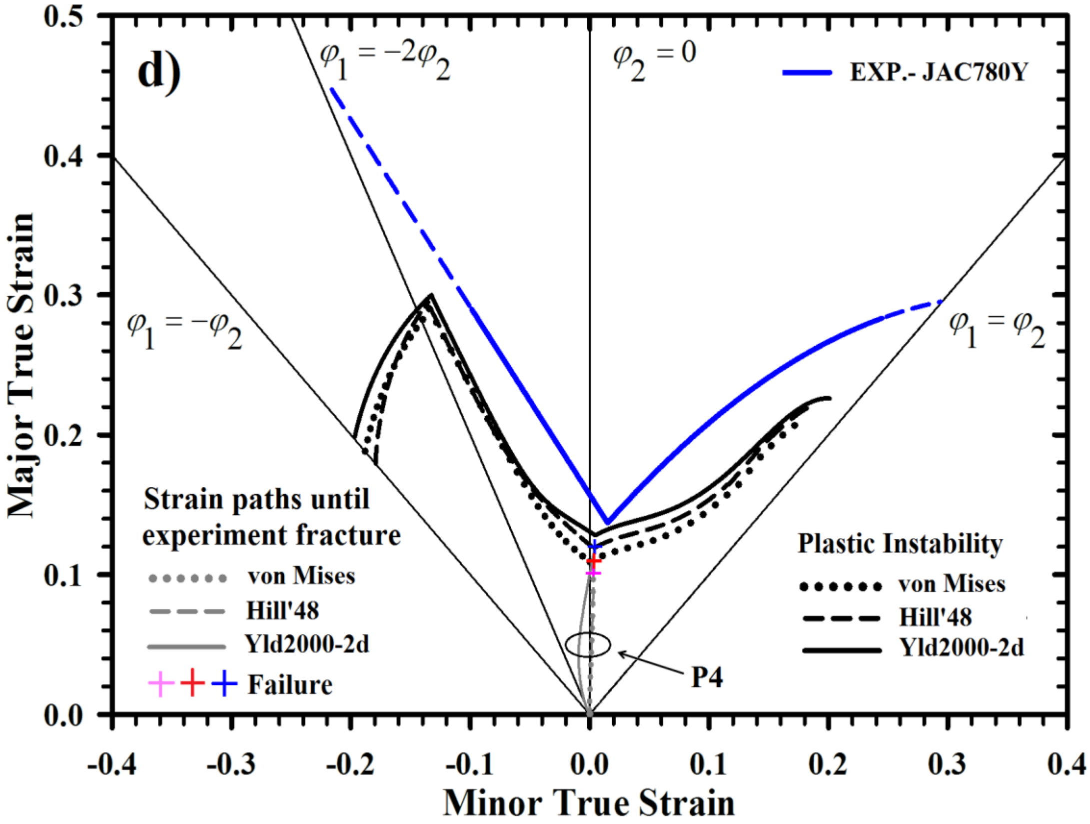

**Figure 6.24** Strain paths from the area (a) P1, (b) P2, (c) P3 and (d) P4 of the industrial pressed part until experimental fractures calculated by using different yield criteria in the instability DC based FLCs and conventional FLC

## 6.4 Conclusion

The damage criteria based on crack initiation and plastic instability represented in the domain of stress triaxiality and effective plastic strain of the high strength steel grade JAC780Y were determined. Tensile tests of sheet specimens with various geometries and notch shapes in combination with the DCPD method and corresponding FE simulations were carried out. In addition, three yield criteria according to the von Mises, Hill’s 48 and Yld2000–2d coupled with the Swift hardening law were considered by the calculations. The findings of the study could be drawn as following.

- The developed damage curves based on crack initiation and plastic instability exhibited a wide range of the stress triaxiality between 0 and 0.667.
- The damage curves for both crack initiation and plastic instability obtained by the Yld2000–2d model were higher than those from the other yield criteria in the entire stress triaxiality range.
- Applicability of the determined damage curves was verified by Nakazima samples representing different states of stress and an industrial stamping part. Some deviations between stress–strain paths calculated by the yield criteria were found. Attained dome heights of the formed samples were predicted for both states of crack initiation and plastic instability and compared with the experimentally measured results. The crack initiation based DCs could fairly describe void initiation and coalescences observed in the critical areas of the Nakazima samples. The instability predictions were slightly underestimated, but could be conservatively applied to formability evaluation of the investigated DP steel.

- The DCs for crack Initiation and plastic instability were transformed to forming limit curves in the domain of in plane principal strains. The obtained crack initiation and instability DC based FLCs exhibited a broad range of stress state from pure shear to biaxial tension.
- The instability DC based FLCs could more accurately describe macroscopic failures of the Nakazima samples at all states of strain and the industrial stamped part than the conventional FLC. Predicted local stress and strain developments of deformed samples significantly depended on the applied yield functions. The DCs based FLCs are a good conservative predictive tool, which can be commonly used in the industry with additional capability to predict shear fracture failure mode. They are thus suitable for applications in industrial environment.